Published in final edited form as:

*Nature*. 2023 February ; 614(7949): 752–761. doi:10.1038/s41586-022-05670-5.

# Influenza vaccination reveals sex dimorphic imprints of prior mild COVID-19

**Rachel Sparks**[1,10], **William W. Lau**[1,10], **Can Liu**[1,2,10], **Kyu Lee Han**[3], **Kiera L. Vrindten**[1], **Guangping Sun**[1,4], **Milann Cox**[1], **Sarah F. Andrews**[5], **Neha Bansal**[1], **Laura E. Failla**[1], **Jody Manischewitz**[6], **Gabrielle Grubbs**[6], **Lisa R. King**[6], **Galina Koroleva**[3], **Stephanie Leimenstoll**[7], **LaQuita Snow**[7], **OP11 Clinical Staff**[8], **Jinguo Chen**[3], **Juanjie Tang**[6], **Amrita Mukherjee**[3], **Brian A. Sellers**[3], **Richard Apps**[3], **Adrian B. McDermott**[5], **Andrew J. Martins**[1], **Evan M. Bloch**[9], **Hana Golding**[6], **Surender Khurana**[6], **John S. Tsang**[1,3,*]

[1]Multiscale Systems Biology Section, Laboratory of Immune System Biology, NIAID, NIH, Bethesda, MD, USA

[2]Graduate Program in Biological Sciences, University of Maryland, College Park, MD, USA

[3]NIH Center for Human Immunology, NIAID, NIH, Bethesda, MD, USA

[4]Division of Intramural Research, NIAID, NIH, Bethesda, MD, USA

[5]Vaccine Research Center, NIAID, NIH, Bethesda, MD, USA

[6]Division of Viral Products, Center for Biologics Evaluation and Research (CBER), FDA, Silver Spring, MD, USA

[7]Laboratory of Clinical Immunology and Microbiology, NIAID, NIH, Bethesda, MD, USA

[8]See consortium author listing below.

[9]Department of Pathology, Johns Hopkins University School of Medicine, Baltimore, MD, USA

[10]These authors contributed equally

## Abstract

[*]Correspondence (JST): john.tsang@yale.edu.

Author Contributions

Conceptualization: RS, JST; Methodology: WWL, CL, JST; Software and formal analysis: WWL, CL; Investigation: RS, WWL, CL, KLH, NB, JM, GG, JRK, GK, JC, JT, AJM; Resources: RS, WWL, CL, KLV, GS, MC, SFA, NB, LEF, SL, LS, PB, DC, AC, JH, AKM, VM, CP, DS, AM, BAS, RA, ABM, EMB, HG, SK, JST; Data curation: RS, WWL, CL, KLV, MC, NB, LEF; Writing – original draft: RS, JST; Writing – review and editing: RS, WWL, CL, JST; Visualization: RS, WWL, CL; Supervision: RS, HG, SK, JST; Project administration: RS, JST; Funding acquisition: RS, JST. Human study and sample acquisition: RS, KLV, GS, MC, NB, LEF, SL, LS, PB, DC, AC, JH, AKM, VM, CP, DS, AM; Flow cytometry of PBMCs (including influenza-specific cell analyses): KLH with panel designs, reagents, and help from SFA; Whole blood RNA-seq: GK, NB; Influenza microneutralization titers, influenza antibody SPR, and SARS-CoV-2 neutralization titers: JM, GG, LRK, JT; CITE-seq data generation: CL, AJM, JC with help from GK and KLV; PBMC cytokine stimulation experiments: CL. Integrative analysis of flow cytometry, CITE-seq, blood RNA-seq, circulating protein, and antibody data: WWL, CL with conceptual contributions from JST.

Competing Interests

EMB reports personal fees and non-financial support from Terumo BCT, Abbott Laboratories, Tegus and UptoDate, outside of the submitted work. EMB is a member of the United States Food and Drug Administration (FDA) Blood Products Advisory Committee. Any views or opinions that are expressed in this manuscript are those of the author's, based on his own scientific expertise and professional judgment; they do not necessarily represent the views of either the Blood Products Advisory Committee or the formal position of FDA, and do not bind or otherwise obligate or commit either Advisory Committee or the Agency to the views expressed. No other authors report competing interests.

Acute viral infections can have durable functional impacts on the immune system long after recovery, but how they affect homeostatic immune states and responses to future perturbations remain poorly understood[1-4]. Here we use systems immunology approaches, including longitudinal multimodal single cell analysis (surface proteins, transcriptome, and V(D)J sequences), to comparatively assess baseline immune statuses and responses to influenza vaccination in 33 healthy individuals after recovery from mild, non-hospitalized COVID-19 (mean: 151 days after diagnosis) and 40 age- and sex-matched controls who never had COVID-19. At baseline and independent of time since COVID-19, recoverees had elevated T-cell activation signatures and lower expression of innate immune genes in monocytes. COVID-19-recovered males had coordinately higher innate, influenza-specific plasmablast, and antibody responses after vaccination compared to healthy male and COVID-19-recovered females, partly because male recoverees had monocytes with higher IL-15 responses early after vaccination coupled with elevated pre-vaccination frequencies of “virtual memory” like CD8+ T-cells poised to produce more IFNγ upon IL-15 stimulation. In addition, the expression of the repressed innate immune genes in monocytes increased by day 1 through day 28 post-vaccination in recoverees, thus moving towards the pre-vaccination baseline of healthy controls. In contrast, these genes decreased on day 1 and returned to the baseline by day 28 in controls. Our study reveals sex-dimorphic impacts of prior mild COVID-19 and suggests that viral infections in humans can establish new set-points impacting future immune responses in an antigen-agnostic manner.

## Introduction

Examples of long-term immunological effects of both chronic and resolved viral infections have been described, e.g., following recovery from natural acute measles infection there is marked reduction in humoral immunity and increased susceptibility to non-measles infections for months to years[1]. Live vaccines such as BCG and measles can impart “training” effects on innate immune cells such as monocytes and their long-lived progenitors, which could underlie the pathogen non-specific effects of BCG in reducing all-cause mortality in infants[5,6]. COVID-19 can result in persistent clinical sequelae for months after infection, both in hospitalized and mild cases[7]. While the spectrum of clinical manifestations of post-acute COVID-19 syndrome (a.k.a “long COVID”) is expanding, our understanding of the molecular and cellular immunological changes after recovery from SARS-CoV-2 infection is lacking. A better understanding of functional immune imprints of mild COVID-19 might have particularly important public health implications given that this population constitutes most COVID-19 recoverees. More broadly, the fundamental issues of whether and how “homeostatic” baseline immune states may have been altered by viral infections, and whether any such alterations may affect responses to future challenges (e.g., infection or vaccination, with shared or distinct antigens) remain poorly understood.

Here we took advantage of a unique opportunity and unprecedented epidemiological environment during the early fall of 2020, months after the first wave of COVID-19, when those with mild COVID-19 had recovered clinically, but before they could be reinfected by SARS-CoV-2 or receive COVID-19 vaccination (which was not available until late 2020); additionally, the prevalence of other respiratory infections was extremely low during this time[8]. We enrolled and comparatively assessed healthy individuals who: 1) recovered from

non-hospitalized, mild cases of COVID-19, and 2) age- and sex-matched controls who never had COVID-19, all from the same geographic region. In addition to assessing the post-COVID-19 immunological statuses, we utilized influenza vaccination to evaluate the immune responses of these two populations at the serological, transcriptional, proteomic, and cellular levels. These analyses reveal basic principles regarding what happens to the immune system after two well-defined immunological encounters in humans: mild COVID-19 as a natural infectious perturbation and influenza vaccination as a controlled and timed intervention with non-SARS-CoV-2 antigens.

## Results

Individuals with prior symptomatic SARS-CoV-2 infection (n=31; diagnosed by nasal PCR test) or asymptomatic infection (n=2; by antibody test, see Methods) during early 2020, and age- and sex-matched healthy controls (HC; n=40) with no history of COVID-19 (and negative by antibody test) were recruited from the community during the fall of 2020 and followed longitudinally (Fig. 1a, see Methods). The average time since COVID-19 diagnosis was 151 days for recoverees (COVR) (Extended Data Fig. 1a; Extended Data Table 1), who had clinically mild illness during acute disease that did not require hospitalization (self-reported average length of illness: 16.5 days) and no major medical comorbidities, including infection at the time of enrollment, obesity (BMI > 30) or autoimmune disease (Fig. 1b). None of the participants were enrolled in COVID-19 vaccine trials, nor did they receive recent vaccination of any kind before administration of the seasonal influenza vaccine in this study. A small number of individuals continued to have mild self-reported sequelae from their illness at study enrollment (3 males and 8 females), the most common being loss of taste and/or smell (Extended Data Table 1). Females were more likely to have sequelae (Fisher's exact test $p = 0.09$ for all subjects, $p = 0.03$ for those < 65 years of age), at a rate similar to that reported in other large studies[9].

### Baseline of mild COVID-19 recoverees

Longitudinal multiomics profiling was performed using whole blood transcriptomics, single cell analysis of 138 surface proteins, transcriptome, and V(D)J sequences via CITE-seq (Cellular Indexing of Transcriptomes and Epitopes by Sequencing[10]), serum protein profiling, antibody characterization, peripheral blood immune cell frequencies with hematological parameters from a complete blood count (CBC), as well as clinical and research flow cytometry covering major immune cell lineages and subsets (Fig. 1b, Supplementary Fig. 1). We first assessed baseline, pre-vaccination differences between the recoverees and the age- and sex-matched HCs. As sex-dependent immune responses to COVID-19 have been reported[11], our analyses explicitly searched for sex-dependent signatures. Immunological resolution following infection may unfold over time even after symptoms subside, and there were indeed parameters that showed evidence of continued evolution in our cohort—defined as those that were correlated with time since COVID-19 diagnosis (TSD; Supplementary Table 1, see Methods), including, as expected, SARS-CoV-2 neutralizing antibody titers[12] (Extended Data Fig. 1b). However, we were primarily interested in uncovering persistent, TSD-independent post-COVID-19 immune imprints, and thus we focused on "temporally stable" immune states associated with prior mild COVID-19

but *not* correlated with TSD. We thus evaluated differences between 1) COVR females (COVR-F) vs. HC females (HC-F); 2) COVR males (COVR-M) vs. HC males (HC-M); and 3) COVR-M vs. COVR-F after accounting for male-female differences in HCs (herein referred to as "sex differences"; Supplementary Table 2). The frequencies of myeloid cells such as monocytes and conventional/myeloid dendritic cells (cDCs) tended to be higher in COVR-M than HC-M and/or COVR-F (Fig. 1c,d; Extended Data Fig. 1c,d), consistent with reports of myeloid cell disruption in COVID-19, particularly in severe, acute disease[13]. Here male-specific elevation in monocyte frequencies was detected even months after recovery from mild disease.

Whole blood transcriptomic (WBT) data also revealed sex-dependent signatures associated with prior COVID-19 (Extended Data Fig. 1e; e.g., the monocyte-related M11.0 and M4.0 from the blood transcriptional module [BTM] collection), including metabolic signatures such as oxidative phosphorylation (Supplementary Table 3). WBT differences can be driven by both cell composition and cell intrinsic transcriptional changes. Indeed, the innate immune, metabolic, and T-cell-related signatures are driven, at least in part, by the increased circulating monocyte and correspondingly lower T-cell frequencies in COVR-M (Fig. 1d and Extended Data Fig. 1f) because these transcriptional enrichment signals became statistically insignificant when monocyte frequencies were taken into account (data not shown).

To assess transcriptional alterations independent of cell frequencies, we used CITE-seq to examine cell type-specific contributions underlying the WBT signatures seen above. We clustered single cells and annotated the resulting clusters using surface protein expression profiles (Fig. 1e; see Methods). Cell type-specific transcriptional analysis pointed to both sex-dependent and -independent differences between COVR and HCs (Supplementary Table 4). Among the enriched gene sets from the WBT analysis above (Extended Data Fig. 1e), but now free of cell-frequency confounding, the BTM M11.0/4.0 gene sets exhibit depressed expression in both classical and non-classical monocytes in COVR relative to HCs in both sexes, while the converse is true for genes in the T-cell activation signature (BTM M7.3) in both CD8+ central memory and effector memory (EM) T-cells (Fig. 1f-i; Extended Data Fig. 1g; Supplementary Table 5); the T-cell activation signature in CD8+ EMs was particularly pronounced in COVR-M (Fig. 1i). The genes driving the monocyte repression enrichment [i.e., the so-called "leading edge genes" (LEGs)] include numerous surface receptors, such as those encoding pattern recognition receptors (TLR2, TLR4, and TLR8), the peptidoglycan recognizing receptor NOD2, the high affinity IgE FC receptor FCER1G, and C-type lectin receptor CLEC4A (Fig. 1f,g). This "innate immune receptor" (IIR) signature in the monocytes, as well as the T-cell activation signature, are predominantly not associated with TSD in both males and females (Extended Data Fig. 1h).

The T-cell activation signature likely emerged during and persisted after acute COVID-19[14], but this was less clear for the IIR signature. We thus asked whether this signature could be linked to gene expression changes seen in acute COVID-19. Using a previously published CITE-seq dataset we generated from a hospitalized, older, and male-biased severe COVID-19 cohort from Italy[15], we noted that within the classical monocytes, the average expression of the IIR LEGs from above was significantly lower in acute COVID-19 patients than healthy controls and was negatively associated with disease severity (Extended Data

Fig. 1i). Thus, this depressed IIR signature could have originated from and stably persisted since the acute response to the infection. Previous studies have reported several (potentially overlapping) types of altered monocytes in acute COVID-19, including those with lower antigen presentation, depressed NF-kB/inflammation, or myeloid-derived suppressor cell (MDSC)-like phenotypes[13,16,17]. However, none of these monocyte phenotypes were significantly different in the monocytes of COVR compared to HCs in our cohort at baseline before influenza vaccination (Supplementary Fig. 2), suggesting that our depressed monocyte gene signature involving pattern recognition and IIR genes is distinct from those identified earlier in acute disease. Together, our findings suggest that even mild, non-hospitalized SARS-CoV-2 infections may establish new, temporally stable, sex-dependent immunological imprints.

To assess whether other natural respiratory viral infections may leave similar unresolved sex-specific “immune states”, we used a published whole blood transcriptomic dataset assessing two independent cohorts of patients with confirmed community influenza A (predominantly pandemic H1N1) infection during two different seasons (2009-2010 and 2010-2011; Extended Data Fig. 2a)[18]. By comparing the WBT profiles before and after each season (i.e., before infection and post-recovery), we found robust post-infection changes consistent between these two independent cohorts in males only (the changes in females were not consistent between these two cohorts; Extended Data Fig. 2b; Supplementary Table 6). The genes with increased expression after recovery in males were also enriched for genes more highly expressed in COVR-M compared to COVR-F in our cohort (after accounting for the expected sex differences present in healthy subjects; Extended Data Fig. 2c). In addition, the genes with lower expression after recovery from influenza infection in males were enriched for the depressed IIR signature above, including TLR5 and VCAN (Fig. 1f,g; Supplementary Table 6). These observations provide independent support that exposure to a respiratory viral pathogen can lead to persistent immunological imprints detectable in blood, even in healthy individuals with mild disease. However, different viral infections are also likely to leave pathogen-dependent imprints with distinct genes and processes; for example, the overlapping signals between post-influenza and post-mild COVID-19 are only a small subset of the sex-specific post-COVID-19 changes we detected.

## Contrasting influenza vaccination responses

We next asked whether prior COVID-19 may impact an individual’s response to non-SARS-CoV-2 immunological challenges. Study participants received the seasonal influenza quadrivalent vaccine and were followed longitudinally for up to 100 days, including days 1, 7, and 28, to assess the vaccine response at the serological, molecular, and cellular levels (Fig. 1a, 1b, 2a). This vaccine was selected in part due to its public health importance: the 2020-21 influenza season was approaching at the start of our study and it was not clear whether prior COVID-19 infection would impact influenza vaccine responses. In addition, the responses to seasonal influenza vaccination have been well characterized in healthy adults, including early innate/inflammatory and interferon (IFN) responses on day 1 (D1) after vaccination and a strong but transient plasmablast peak around day 7 (D7) culminating in the generation of influenza-specific antibodies[19,20]. Thus, influenza

vaccination provides an excellent perturbation to probe the functional impacts of prior mild SARS-CoV-2 infection.

Blood transcriptomic, peripheral immune cell frequency, CITE-seq, influenza-specific B-cell, and antibody titer analyses [assessing responses on D1, D7 and day 28 (D28) relative to day 0 (D0)] together pointed to coordinated, sex-specific innate and adaptive response differences to the vaccine, with COVR-M generally mounting a more potent response than their healthy counterparts and COVR-F (Fig. 2b-i and Extended Data Fig. 3a, 3c-g; Supplementary Tables 7 and 8). These include stronger innate/inflammatory and particularly IFN-related transcriptional responses (Fig. 2b, Extended Data Fig. 3a), with corresponding greater increases in circulating IFNγ protein levels in serum by D1 in COVR-M (Fig. 2c). This systemic increase in IFNγ impacts diverse cell types expressing the IFNγ signaling components as revealed by single cell CITE-seq: most peripheral immune cells had higher IFN response signatures on D1 in COVR-M than the other groups (based on comparing D1 vs. D0; Fig. 2d; Fig. 2e shows CD4+ T-cells, B-cells, monocytes and cDCs as examples). Baseline, pre-vaccination IFN-related transcriptional activity was largely indistinguishable between COVR and HC (Extended Data Fig. 3b). In addition, a more robust response was observed for antigen presentation genes including both MHC class I and II genes in classical monocytes of COVR-M (Fig. 2f). Thus, COVR-M mount a stronger circulating IFNγ and corresponding transcriptional response in both innate and adaptive immune cells by D1 following influenza vaccination.

Based on previous studies of influenza vaccination in healthy adults and because heightened innate immune responses elicited by adjuvants are known to enhance adaptive responses[21], we hypothesized that the stronger early inflammatory responses in COVR-M would lead to a more robust humoral response. Indeed, we saw increased D7 B-/plasma-cell related transcriptional signatures in the COVR-M (Extended Data Fig. 3a,c). Furthermore, COVR-M had a greater increase of influenza-specific plasmablasts than HC-M at D7 (Fig. 2g, Supplementary Fig. 3). Consistent with previous observations in healthy adults[22] and the hypothesis that the stronger early IFN response in COVR-M could help induce a more robust B-cell response, we detected a positive correlation between those two parameters, including the extent of influenza-specific plasmablast increases (Extended Data Fig. 3d). Consistently, COVR-M also had higher influenza-specific antibody responses than HC-M across all but one of the vaccine strains at D28 relative to baseline (Fig. 2h,i; Extended Data Fig. 3e-g; Supplementary Table 8; see Methods). While influenza infection and vaccination history can influence influenza vaccine responses[23], they alone are unlikely to explain the above findings as the COVR and HC groups had similar baseline antibody titers (Extended Data Fig. 3e,f), were age/sex-matched, and drawn from the same geographic region with very low influenza infection/transmission during the 2020-21 season[8]. Additionally, the statistical model used to assess titer response differences incorporated pre-vaccination influenza titers as a covariate (see Methods). The extent of time-dependent immune resolution following COVID-19 was unlikely a factor because TSD and D28 titer responses are not correlated in either sex (data not shown). Together, these observations demonstrate that prior mild infection by SARS-CoV-2 can result in sex-dependent, coordinated changes in both innate and adaptive responses to immunization with non-SARS-CoV-2 antigens months after acute disease.

### Linking baseline to innate response

Having established that prior mild COVID-19 is associated with new baseline immune states prior to influenza vaccination (Fig. 1 and Extended Data Fig. 1) and COVR-M-specific responses following vaccination (Fig. 2 and Extended Data Fig. 3), we next attempted to link the two and asked what baseline variables and cellular circuits may contribute to the heightened IFN-related responses in COVR-M, which could subsequently contribute to the more robust humoral responses in COVR-M (Fig. 3a). Using flow cytometry (Supplementary Fig. 1) and CITE-seq data, we first employed a multivariate linear model to identify baseline/pre-vaccination immune cells whose frequency predicted the D1 IFN-related responses (D1 vs. D0 in serum IFNγ protein levels and IFN transcriptional signature score). A subset of CD8+ T-cells with an effector memory (CD8 EM) phenotype (CD45RA− CCR7− CD28+ CD27−; “early effector-like”) was a top candidate in COVR-M and could thus be a cellular source of IFNγ upon vaccination (Extended Data Fig. 4a,b; Supplementary Fig. 4); the same relationship was not observed in HCs (Supplementary Fig. 5a,b).

We next focused on all the CD8+ T-cells from clusters with an EM phenotype (CD8 EM) in the CITE-seq data based on both surface protein markers and mRNA expression (see Methods and Supplementary Table 10 for the top cluster protein markers). We searched for differences in average surface marker expression of cells in these CD8 EM clusters across the four subject groups and found that GPR56 was the top differentially expressed marker with increased expression in COVR-M relative to the HC-M and COVR-F (Fig. 3b,c; Supplementary Table 10). This was intriguing because CD4+ EM andTEMRA (EM cells re-expressing CD45RA) T-cells marked by surface GPR56 expression at baseline (before stimulation) have been reported to produce increased amounts of IFNγ upon PMA/ionomycin (PMAI) stimulation[24]. Consistent with this, GPR56+ CD8 EM cells in our data are enriched for a transcriptional signature (derived in an independent study[25]) that marks CD8 EM cells poised to secrete higher levels of IFNγ upon PMAI stimulation (Fig. 3d). Thus, GPR56+ CD8 EM cells could be a source of elevated IFNγ production in COVR-M following influenza vaccination. Indeed, the frequency of these cells was elevated in COVR-M relative to both HC-M and COVR-F prior to vaccination (Fig. 3e), but not correlated with the TSD and thus temporally stable (assessed by Spearman’s correlation: p value = 0.18 in COVR-F and p value = 0.51 in COVR-M). Additionally, IFNG transcripts increased significantly in these cells on D1 following influenza vaccination in COVR-M (Extended Data Fig. 4c,d). These data suggest that prior COVID-19 increases the frequency of GPR56+ CD8 EM cells in males and these cells are poised to make more IFNγ early after influenza vaccination, which together contributed to the higher IFNγ production in COVR-M; consistent with this hypothesis, this was not observed in GPR56− cells (Extended Data Fig. 4d; Supplementary Fig. 5c).

Mild, non-hospitalized COVID-19 has been reported to induce “bystander activation” (non-SARS-CoV-2 specific) of CD8+ T-cells[26]. Interestingly, the GPR56+ cells are also enriched for a transcriptional signature associated with bystander T-cell activation[26,27] (Fig. 3f). In addition, GPR56+ CD8 EM cell frequency is positively correlated with the T-cell activation signature score, which was elevated at baseline in COVR-M as shown above (Fig. 1i, Extended Data Fig. 4e). This suggests that some of these cells may have

expanded in a bystander manner during the acute phase of the infection. This prompted us to consider whether these GPR56+ cells are similar to bystander-activated virtual memory (VM) CD8+ T-cells, a feature of which is their ability to be activated rapidly by inflammatory cytokines alone (e.g., IL-12, IL-18, and IL-15) to produce IFNγ without T-cell receptor (TCR) stimulation[28,29]. VM CD8+ T-cells expand via cytokine stimulation, including IL-15 induced by viral infection (IL-15 concentrations are known to be elevated in acute COVID-19 patients and correlate with disease severity[30]), and are characterized by a differentiated EM phenotype expressing CD45RA[28]. We assessed several reported surface markers of these cells[28] in GPR56+ vs. GPR56− cells and found that the GPR56+ cells were indeed phenotypically similar to VM cells (Fig. 3g). For example, GPR56+ cells have higher CD122 but lower CD5 surface expression than their GPR56− counterparts; the latter of which has been linked to the extent of prior IL-15 (or potentially other inflammatory cytokine) encounters[28,31]. Interestingly, based on the surface levels of CD45RA and CD45RO, the GPR56+ cells appear to situate phenotypically between GPR56− and TEMRA cells (Extended Data Fig. 4f).

To further test our hypothesis, we performed *in vitro* stimulation experiments to assess whether GPR56+ CD8+ T-cells can produce IFNγ in response to several cytokines known to be induced by vaccination or infection (Supplementary Fig. 6a). Stimulation with IL-15 showed that GPR56+ CD45RA+ CD8+ T-cells from COVR-M produced more IFNγ compared to COVR-F (Fig. 3h,i). CD8+ VM-like T-cells were identified using surface markers CD45RA+, KIR+ and/or NKG2A+[32,33] and COVR-M produced higher IFNγ in these cells (Fig. 3i). Stimulation with IL-12, IL-15, and IL-18 together showed similar trends (Supplementary Fig. 6b). Stimulation with IL-18 alone or IL-12 and IL-18 together also showed similar trends, but these conditions induced less robust IFNγ than IL-15 stimulation (data not shown). We next assessed the cellular source of IL-15 post influenza vaccination using CITE-seq data and found that classical monocytes from COVR-M showed the most significant increases in IL-15 mRNA levels on day 1 after influenza vaccination (Fig. 3j). Together this suggests that the increased IFNγ response in COVR-M following vaccination could be attributed to increased baseline (pre-vaccination) frequencies in cells that are also intrinsically more responsive to inflammatory stimulation, including classical monocytes that produce elevated IL-15 and CD8 VM-like T-cells that mount a more robust IFNγ response to cytokine stimulation alone.

Since VM T-cells can be rapidly activated to produce cytokines without clonal, antigen-specific expansion[28], we assessed the clonality of the GPR56+ CD8 EM cells at different timepoints after influenza vaccination using V(D)J/TCR data from CITE-seq. The clonality of both the GPR56+ CD8 EM and TEMRA cells remained stable across days 0 (before vaccination), 1 and 28 following influenza vaccination (Extended Data Fig. 4g,h). The frequencies of GPR56+ CD8 EM clones shared across timepoints within individuals were also similar (Extended Data Fig. 4i). Together, these data argue against the notion that the heightened activation of the GPR56+ cells early after influenza vaccination in COVR-M was due solely to TCR-dependent T-cell activation and clonal expansion. As was shown previously[28,29] and above in our *in vitro* stimulation data, a more plausible explanation is that these CD8+ VM-like cells were activated to produce IFNγ by the inflammatory cytokines elicited by the influenza vaccine in an antigen-independent manner. Despite their

resemblance to VM cells, some of the GPR56+ cells could have developed from naïve cells via conventional, non-bystander pathways (e.g., some could be developed during acute COVID-19 and are specific for SARS-CoV-2), although none of these cells had a CDR3 sequence that matches a public clone deemed to be specific for SARS-CoV-2 (data not shown). Bona fide, antigen-specific memory CD8+ T-cells developed from naïve cells via TCR stimulation have also been shown to produce IFNγ in response to inflammatory cytokines alone in mice[34,35].

Our data also revealed other cell types that could have contributed to the increased IFNγ production observed on D1 after vaccination in COVR-M (Supplementary Fig. 7a-c). IFNG transcript increased more in COVR-M than HC-M and COVR-F on day 1 in $CD16^{lo}$ NK cells (Supplementary Fig. 7c, Supplementary Table 4). Additionally, the baseline frequency of $CD16^{lo}$ NK cells was correlated with the extent of D1 increase in both IFNG expression and serum protein levels (Supplementary Fig. 7b). However, the IFNγ response in total NK cells after IL-15 stimulation *in vitro* was not significantly higher in COVR-M (Extended Data Fig. 4j), likely because $CD16^{lo}$ NK cells are a small subset of total NK cells. In contrast, IL-15 stimulation *in vitro* revealed a higher IFNγ response in MAIT cells in COVR-M than both COVR-F and HC-M (Extended Data Fig. 4j), but the IFNG mRNA expression increase on D1 post influenza vaccination was not statistically significant in COVR-M based on CITE-seq data (Supplementary Fig. 7c). CD8+ T-cells with a TEMRA (CD45RA+ CD45RO− CCR7−) phenotype might also play a role as their IFNγ response after IL-15 stimulation *in vitro* was higher in COVR-M than both COVR-F and HC-M (Extended Data Fig. 4j), which is consistent with CITE-seq data (Supplementary Fig. 7c).

Taken together, we demonstrate a population of CD8 EM T-cells marked by GPR56 expression and VM-like markers with antigen-agnostic pro-inflammatory potential after heterologous vaccination. Importantly, these cells, and potentially $CD16^{lo}$ NK, MAIT, and CD8+ TEMRA cells (albeit with less support from our CITE-seq data), emerged in otherwise clinically healthy individuals and are especially elevated and more poised to respond in males who were months recovered from mild SARS-CoV-2 infection, providing additional evidence for sex-specific, functionally relevant immune set points linked to prior mild COVID-19.

## Vaccination shifts monocyte imprints

Given the potential for vaccine-induced “training” effects[6,36,37], we next asked whether influenza vaccination can alter some of the post-COVID-19 transcriptional imprints we detected earlier (Fig. 4a). We focused on the monocytes because of the robustly depressed IIR signature reported above (in COVR vs. HC; Fig. 1f,g) and because vaccines can potentially induce long-lasting changes in these cells[6,36]. By using the HC baseline (D0) as a healthy reference, we used CITE-seq data to assess the average expression of the signature genes (identified above) before and after vaccination in COVR subjects, separately for classical (Fig. 1f) and non-classical monocytes (Fig. 1g) in males and females (Extended Data Fig. 5a,b). As was observed above, these genes had lower average expression in COVR than HC in both sexes at D0 before vaccination. However, their average expression increased

towards that of the HCs by D1 and persisted through D28 in both COVR-F and COVR-M, although the effect appeared stronger in COVR-F (Extended Data Fig. 5a,b).

Quantifying the average expression (module score) of these sex- and cell type-dependent gene sets (Fig. 1f,g) within individual subjects over time confirmed a similar and significant trend of shift towards the HCs (Fig. 4b,c). This analysis further revealed that the extent of this change in gene expression was more pronounced in the non-classical than the classical monocytes (Fig. 4b,c). Intriguingly, the behavior of these genes was divergent in the HCs: the gene module score trended lower on D1 and reverted to pre-vaccination levels by day 28 in HCs (Fig. 4b,c). While the underlying mechanism of this divergence is unclear, the monocytes in HCs could have responded to the vaccine-induced inflammation by downregulating certain immune receptor and associated signaling genes in a negative feedforward mechanism to avoid over responding, while the “depressed” monocytes in COVR instead responded by increasing the expression of these genes and thus moving towards the normal (healthy baseline) level.

We next identified the individual genes within these gene sets that moved towards the HC baseline (see Methods). In both classical and non-classical monocytes, the fraction of reverting genes was significantly higher in females than males (Fig. 4d,e; Extended Data Fig. 5c), although several TLRs (e.g., TLR2, TLR4) and NOD2 were significant in both sexes in one or both monocyte subsets. These changes were unlikely due to continued immune resolution following infection because the baseline (D0) expression of these genes did not correlate with TSD (Extended Data Fig. 1h), and they increased acutely by D1 following vaccination and persisted to D28. Interestingly, unlike this depressed IIR signature (Fig. 1f,g, Extended Data Fig. 1i), other monocyte-related transcriptional signatures known to have lower expression during acute COVID-19, such as genes related to antigen presentation, inflammatory and NF-kB activation, and myeloid suppressor cells[13,15-17,38,39], were similar between COVR and HC at D0/baseline; vaccination also did not consistently elicit longer-lasting changes in these signatures out to D28, although COVR-M tended to have elevated antigen presentation transcriptional responses in non-classical monocytes on D1 that remained mildly elevated by D28 (Extended Data Fig. 5d,e).

Together, CITE-seq analysis revealed that the early (D1) response to influenza vaccination elevates a set of previously (i.e., before vaccination) depressed IIR genes in the monocytes of COVR subjects out to at least D28 post vaccination. Although the functional relevance of these changes remains to be determined, these results suggest that the early inflammatory responses to influenza vaccination can help to shift the post-COVID-19 immune state of monocytes towards that of healthy, particularly in female recoverees.

## Discussion

While both acute and longer-term immune perturbations in hospitalized COVID-19 patients have been reported[13,40-43], less is known regarding healthy recovered individuals with prior mild, non-hospitalized SARS-CoV-2 infection months after acute illness, without confounding comorbidities such as obesity, autoimmunity, or immunodeficiency. Here we reveal that clinically healthy recoverees of prior non-hospitalized COVID-19 possess sex-

specific immune imprints beyond SARS-CoV-2 specific immunity, some of which only become apparent after vaccination with antigens distinct from SARS-CoV-2. Our findings are consistent with the sex dimorphic nature of acute responses to SARS-CoV-2 and other immune challenges[11]. Healthy females tend to mount heightened inflammatory responses to infections and vaccines[44]; it was therefore surprising to find the qualitative opposite here in which COVR-M were found to have a more “poised” immune status at baseline and stronger innate and adaptive responses to influenza vaccination. While persistent immune state changes (over months) in patients with “long COVID” have been reported[41], most of the individuals in our study reported no or minor post-COVID-19 sequelae. Future work could assess whether some of the sex-specific imprints, including differences in vaccination responses, are associated with “long COVID”[7].

Our findings suggest that the “poised” baseline immune states in COVR-M helped establish the more robust IFN, plasmablast, and antibody responses on days 1, 7, and 28, respectively, following influenza vaccination. The early IFN responses may be attributed to monocytes with higher IL-15 responses early after vaccination coupled with elevated pre-vaccination frequencies of “virtual memory” like CD8+ T-cells poised to produce more IFNγ upon IL-15 stimulation. The monocyte imprint we described involving poised IL-15 mRNA production in male recoverees and the transcriptionally depressed innate receptor gene signature in both sexes are consistent with the notion of trained innate immunity[6]. Interestingly, while the latter signature could be detected in acute COVID-19 patients with severe disease, it is distinct from the depressed antigen presentation or myeloid suppressor cell like states found in earlier studies[13,15-17,38,39]. As trained innate immunity can be mediated through myriad mechanisms including chromatin and metabolic changes within cells, future studies could explore these potential mechanisms in monocytes, including the influences of sex/gender, acute disease severity, and age among subjects with a range of post-COVID clinical sequelae. Given that the half-life of circulating monocytes is relatively short (and can be shorter than 28 days)[45], the partial reversal we detected is possibly attributable to bone marrow myeloid progenitor cells, as hematopoietic stem and progenitor cells have been shown to exhibit chromatin accessibility changes following SARS-CoV2 infection[46].

Bystander T-cell activation has been reported following natural viral infections[47], including SARS-CoV-2[26]. More recently, bystander activated CD8 EM T-cells have been identified as playing an important role in controlling early infection, including VM cells that have no prior antigen exposure or TCR engagement[28,29]. As these cells can emerge following cytokine stimulation alone, it is possible that a stronger or more prolonged cytokine response to SARS-CoV-2 in males relative to females during acute disease may have resulted in the elevated frequencies of the GPR56+ CD8+ VM-like cells in COVR-M. This hypothesis is consistent with reports that males hospitalized with COVID-19 tend to experience greater innate immune activation (as measured by circulating cytokines) compared to females[48,49].

Some of the immune imprints we observed could be shared among different types of viral infections, but some are likely unique to SARS-CoV-2, as suggested by our comparison with natural influenza infection. Our findings point to the possibility that any infection or immune challenge may change the immune status to establish new baseline set points encoded by

the states of not only a single cell lineage, but a network of interacting cell types such as VM T-cells and monocytes. In addition, while baseline immune statuses predictive of future responses are often different across and temporally stable within individuals over a timescale of months[50,51], our results suggest that such baseline immune states could have been established by past infections and are stable up to the next perturbation. Thus, the baseline immune status of an individual, with the potential to impact future responses in both antigen-specific and -agnostic ways, is shaped by a multitude of prior exposures[2,3]. In addition to revealing underlying principles regarding what happens after two well-defined natural immunological encounters: mild COVID-19 and influenza vaccination in humans, our observations provide a basis for studying more complex scenarios, such as what happens over longer timescales with additional encounters. Our work brings forth the concept that even mild viral infections could establish new immunological set-points impacting future immune responses in an antigen-agnostic manner and illustrates how heterologous vaccination could be used as a tool to reveal such functional imprints.

**Limitations of this study** and additional discussion can be found in the Supplementary Information.

## Methods

### Patient population and sample collection

Subjects at least 18 years of age were recruited between August and December 2020 from the local area (Maryland, Virginia, and the District of Columbia) and enrolled on National Institutes of Health (NIH) protocol 19-I-0126 (Systems analyses of the immune response to the seasonal influenza vaccine). The study was approved by the NIH Institutional Review Board (ClinicalTrials.gov ID: NCT04025580) and complied with all relevant ethical regulations. Informed consent was obtained from all participants. After informed consent, a baseline history and physical examination were performed. Subjects were asked to characterize any present, persistent symptoms of past SARS-CoV-2 infection. Exclusion criteria included obesity (BMI ≥ 30); history of or suspicion of any autoimmune, autoinflammatory or immunodeficiency disease; history of any vaccine within the past 30 days (live attenuated) or 14 days (non-live attenuated); history of any experimental vaccine; history of a parasitic, amebic, fungal, or mycobacterial infection in the past year; or current infection. The COVID-19 vaccine was not available at the time of the study, and no study participants participated in any COVID-19 vaccine trials. All study visits occurred at the NIH Clinical Center (CC) in Bethesda, Maryland, USA. Blood samples were collected by phlebotomy staff at the NIH CC. Samples were collected between September 2020 and April 2021.

Samples were collected on subjects from three groups: 1) those with a prior history of symptomatic SARS-CoV-2 infection (defined as a history positive nasal PCR test and positive Food and Drug Administration (FDA) Emergency Use Authorization (EUA) SARS-CoV-2 antibody test at the time of protocol screening), 2) those with a history of asymptomatic SARS-CoV-2 infection (defined as a positive FDA EUA SARS-CoV-2 antibody test at the time of protocol exam but no history of COVID-like symptoms; no time since COVID-19 infection or diagnosis (TSD) was identifiable for this group and they

were excluded from all TSD analyses), and 3) individuals with no history of SARS-CoV-2 infection (defined as a negative FDA EUA SARS-CoV-2 antibody test at the time of the protocol screening).

Blood for PBMCs, serum, whole blood RNA [Tempus™ Blood RNA Tube (Thermo Fisher Scientific, Waltham, MA)], complete blood count with differential (CBC) and lymphocyte phenotyping was collected at each of the following timepoints relative to seasonal influenza vaccination (day 0): days −7, 0, 1, 7, 14, 28, 70, 100. Optional stool was collected at days 0, 28 and 100. Subjects were provided with Cardinal Health Stool Collection kits (Cardinal Health, Dublin, OH) and Styrofoam storage containers with ice packs to collect stool samples at home and return in person to the NIH. Following day 100, subjects had the option to continue to provide monthly blood samples for PBMCs, serum, whole blood RNA, CBC with differential and lymphocyte phenotyping through August 2021.

At each timepoint following study enrollment, data were collected and managed using REDCap (v8.5.27) electronic data capture tools hosted at the NIH[52,53]. REDCap (Research Electronic Data Capture) is a secure, web-based software platform designed to support data capture for research studies, providing 1) an intuitive interface for validated data capture; 2) audit trails for tracking data manipulation and export procedures; 3) automated export procedures for seamless data downloads to common statistical packages; and 4) procedures for data integration and interoperability with external sources. REDCap electronic questionnaires were utilized to collect information from participants via two separate IRB-approved surveys. A survey to evaluate vaccine-related adverse events or symptoms was administered on study days 1 and 7 and a separate survey to evaluate for any health changes or new medications was administered at every visit starting on Day 0. Surveys were sent via email to the participants and responses were transferred from the REDCap system to the NIH Clinical Research Information Management System (CRIMSON) system by the study team.

### Influenza vaccination

Subjects between ages 18 – 64 years were administered the Flucelvax Quadrivalent seasonal influenza vaccine (2020-2021; Seqirus Inc, Summit, NJ). Subjects 65 years of age and older were administered the high-dose Fluzone Quadrivalent seasonal influenza vaccine (2020-2021; Sanofi Pasteur Inc, Swiftwater, PA).

### Influenza microneutralization titers

Virus-neutralizing titers of pre- and post-vaccination sera were determined in a microneutralization assay based on the methods of the pandemic influenza reference laboratories of the Centers for Disease Control and Prevention (CDC) using low pathogenicity vaccine viruses and MDCK cells. The X-179A virus is a 5:3 reassortant vaccine containing the HA, NA, and PB1 genes from A/California/07/2009 (H1N1pdm09) and the 5 other genes from A/PR/8/34 were donated by the high growth virus NYMC X-157. Immune sera were also tested for neutralization titers of the seasonal vaccine strains H1N1 A/Brisbane/59/07, H3N2 A/Uruguay/716/07, and B/Brisbane/60/2001. Internal controls in all assays were sheep sera generated against the corresponding strains at the Center for

Biologics Evaluation and Research, FDA, Bethesda, MD. All individual sera were serially diluted (2-fold dilutions starting at 1:10) and were assayed against 100 TCID50 of each strain in duplicates in 96-well plates (1:1 mixtures). The titers represent the highest dilution that completely suppressed virus replication.

### SARS-CoV-2 pseudovirus production and neutralization assay[54-56]

Human codon-optimized cDNA encoding SARS-CoV-2 S glycoprotein (NC_045512) was cloned into eukaryotic cell expression vector pcDNA 3.1 between the *BamH*I and *Xho*I sites. Pseudovirions were produced by co-transfection of Lenti-X 293T cells with psPAX2(gag/pol), pTrip-luc lentiviral vector and pcDNA 3.1 SARS-CoV-2-spike-deltaC19, using Lipofectamine 3000. The supernatants were harvested at 48h post transfection and filtered through 0.45-μm membranes and titrated using 293T-ACE2 cells (HEK293T cells that express ACE2 protein). The following reagent was obtained through BEI Resources, NIAID, NIH: Human Embryonic Kidney Cells (HEK-293T) Expressing Human Angiotensin-Converting Enzyme 2, HEK-293T-hACE2 Cell Line, NR-52511.

For the neutralization assay, 50 μL of SARS-CoV-2 S pseudovirions were pre-incubated with an equal volume of varying dilutions of serum at room temperature for 1 h, then virus-antibody mixtures were added to 293T-ACE2 cells in a 96-well plate. After 3 h incubation, the inoculum was replaced with fresh medium. After 24 hours, cells were lysed and luciferase activity was measured. Controls included cell only control, virus without any antibody control and positive control sera.

### SPR based antibody binding kinetics of human serum[57-59]

Steady-state equilibrium binding of serum was monitored at 25°C using a ProteOn surface plasmon resonance (BioRad). The purified recombinant SARS-CoV-2 or other proteins were captured to a Ni-NTA sensor chip (BioRad, Catalog number: 176-5031) with 200 resonance units (RU) in the test flow channels. The protein density on the chip was optimized such as to measure monovalent interactions independent of the antibody isotype. Serial dilutions (10-, 30- and 90-fold) of freshly prepared sample in BSA-PBST buffer (PBS pH 7.4 buffer with Tween-20 and BSA) were injected at a flow rate of 50 μL/min (120 sec contact duration) for association, and disassociation was performed over a 600-second interval. Responses from the protein surface were corrected for the response from a mock surface and for responses from a buffer-only injection. Total antibody binding was calculated with BioRad ProteOn manager software (version 3.1). All SPR experiments were performed twice, and the researchers performing the assay were blinded to sample identity. In these optimized SPR conditions, the variation for each sample in duplicate SPR runs was <5%. The maximum resonance units (Max RU) data shown in the figures were the RU signal for the 10-fold diluted serum sample.

### PBMC isolation

PBMC samples were isolated from blood collected in Vacutainer EDTA tubes (generic lab supplier) using the SepMate™-50 tubes (STEMCELL Technologies, Cambridge, MA) with following modifications to the manufacturer's protocol: The blood samples were diluted 1:1 with room temperate PBS and mixed by pipetting. The diluted blood was layered on

top of 15ml Cytiva™ Ficoll™ PAQUE-Plus (Cytiva Life Sciences, Marlborough, MA) layer in SepMate™. The SepMate™ tubes were spun at 1200 g for 10 mins with brake set to 5 at room temperature. Following the spin, the top plasma layer was removed as much as possible without disturbing the PBMC layer. If there were any cells stuck on the wall of the tube, then they were gently scraped from the wall with pipette, so they can be resuspended with rest of the cells. The cells were poured from SepMate™ in to a 50ml conical tube. The tubes containing cells were filled up to 50ml with cold wash buffer (PBS with 2% FBS) and mixed by inverting. The tubes were spun at 300 g for 10 mins with brake set to 5 at room temperature. After the spin, the supernatant was removed without disturbing the cell pellet. After resuspending the pellet with cold wash buffer, the cells were counted using the Guava® Muse® Cell Analyzer (Luminex Corporation, Austin, TX). The tubes were again spun at 300 g for 10 mins with brake set to 5 at room temperature. The supernatant was removed without disturbing the cell pellet.

Based on the cell count, 6 – 10 million PBMC were frozen per vial for each sample. Since the cells were counted prior to the last spin, a 50% cell loss was assumed and accounted for in the calculations from cell count. The cell pellet was resuspended with n*600µl (n = number of PBMC vials to be frozen) freezing media (RPMI with 10% FBS) by gentle pipetting. After freezing media, n*600µl DMSO freeze (FBS with 15% DMSO) was added drop-by-drop while gently shaking the tube. In other words, for each vial of PBMC that was to be frozen, 600µl of freezing media and 600µl of DMSO freeze was added, bringing the total volume for each vial to 1.2ml. The solution was gently mixed by pipetting before transferring 1.2ml cell solution to each 1.8ml cryovial (general lab supplier). The cell vials were placed in CoolCell Containers (Thomas Scientific, Swedesboro, NJ) and the container was placed in a −80°C freezer. After at least 4 hours, the PBMC vials were transferred to liquid nitrogen.

## RNA isolation

Blood was drawn directly into the Tempus™ Blood RNA Tube (Thermo Fisher Scientific, Waltham, MA) according to manufacturer's protocol. Two Tempus tubes were collected at each study timepoint. The blood sample from each Tempus tube was aliquoted in to two 4.5mL cryovials (General lab supplier). These cryovials were directly stored at −80°C.

The RNA samples were isolated in groups of 12-22 samples per batch based on careful batching prior to isolation to reduce confounding factors due to age, gender, and patient group.

RNA was isolated from tempus blood using the QIAsymphony RNA Kit (Qiagen, Gaithersburg, MD) on QIAsymphony SP instrument (Qiagen, Gaithersburg, MD). Blood samples were thawed on ice before each sample was transferred to a 50ml conical tube. The total volume of the sample was brought to 12ml by adding 1x PBS. The tubes were vortexed at full speed for 30 seconds, followed by centrifugation at 3500 g for 1 hour at 4°C. After centrifugation, the supernatant from the tubes was decanted and tubes were placed upside down on clean paper towels for 2 minutes to allow residual liquid to drain. To resuspend the pellet, 800µl of RLT+ buffer was added to the bottom of each tube and vortexed for few seconds. All 800µl of each sample was transferred to 2ml screw cap tubes (Sarstedt,

Nümbrecht, Germany). The tubes were placed into #3b adapters (Qiagen, Gaithersburg, MD) to be loaded on to the QIAsymphony.

On the QIAsymphony, RNA CT 800 protocol was selected and used for RNA isolation. The instrument was set up according to the manufacturer's protocol and the elution volume for RNA samples was set to 100µl. The final volume of the eluted RNA samples ranged from 65 – 95 µl.

RNA yields were determined using Qubit RNA BR kit or Qubit RNA HS kit (Thermo Fisher Scientific, Waltham, MA) based on the yield. RNA RIN numbers were measured using RNA ScreenTape (Agilent Technologies, Santa Clara, CA). The average RIN was 8.3 and average yield was 81.3 ng/µl for the RNA samples.

## RNA-seq

RNA-seq libraries were prepared manually using Universal Plus mRNA-Seq with NuQuant, Human Globin AnyDeplete (Tecan Genomics, Redwood City, CA) according to manufacturer's protocol. For each sample, 500ng of total RNA was used to isolate mRNA via poly(A) selection. Captured mRNA was washed, fragmented, and primed with the mix of random and oligo(dT) primers. After cDNA synthesis, ends were repaired and ligated with Unique Dual Index (UDI) adaptor pairs. Unwanted abundant transcripts from rRNA, mtRNA and globin were removed using AnyDeplete module. Remaining library was amplified by 14 cycles of PCR and purified with AMPure XP reagent (Beckman Coulter, Indianapolis, IN).

Library concentration was determined by Quant-iT™ PicoGreen™ dsDNA Assay kit (Thermo Fisher Scientific, Waltham, MA) on BioTek Synergy H1 plate reader (BioTek Instruments, Winooski, VT) using 2 ul sample. Library size distribution was determined using D1000 ScreenTape (Agilent Technologies, Santa Clara, CA) on 4200 TapeStation System (Agilent Technologies, Santa Clara, CA). Thirty-two samples were randomly selected from each plate to measure the library size distribution. To determine fragment size, the region on the electropherogram was set from 200 bp to 700 bp. An average of the fragment sizes was used for the rest of libraries to calculate molarity.

To create a balanced pool for sequencing, all libraries from one plate were diluted to the same molar concentration by the QIAgility liquid handling robot (Qiagen, Gaithersburg, MD) and equal volumes of normalized samples were pooled. Ninety-six samples were pooled from each plate on Plates 1-4 and 35 samples were pooled from Plate 5. For an accurate quantification of the pooled libraries, a qPCR was performed using KAPA Library Quantification Kit (Roche, Wilmington, MA).

All libraries were sequenced on the NovaSeq 6000 instrument (Illumina, San Diego, CA) at Center for Cancer Research Sequencing Facility, National Cancer Institute. The libraries pooled from Plates 1-4 were sequenced using one NovaSeq 6000 S4 Reagent Kit (200 cycles) and NovaSeq XP 4-Lane Kit (Illumina, San Diego, CA) with sequencing parameter as 100 bp paired-end reads. The library pool from Plate 5 was sequenced using a NovaSeq

6000 SP Reagent Kit (300 cycles; Illumina, San Diego, CA) with 150 bp paired-end reads as sequencing parameter.

Additionally, after quality control, 11 samples were re-sequenced as Plate 6 on a NextSeq 500 instrument using a NovaSeq 6000 S4 Reagent Kit (200 cycles) with sequencing parameter as 100 bp paired-end reads. Technical replicates were placed on each plate to control for plate variability.

## CITE-seq

**a) Single cell CITE-seq processing—**Frozen PBMC samples were thawed, recovered, and washed using RPMI media with 10% FBS and 10mg/mL DNase I (STEMCELL) and then processed as previously described[15] for CITE-seq staining. In brief, samples from different donors were pooled and different timepoints from the same donor were pooled separately so that each pool contains only one timepoint from one donor. PBMC pools were Fc blocked (Human TruStain FcX, BioLegend) and stained with Totalseq-C human 'hashtag' antibodies (BioLegend), washed with CITE-seq staining buffer (2% BSA in PBS). Then hashtagged PBMC pools were combined, and cells were stained with a cocktail of TotalSeq-C human lyophilized panel (BioLegend) of 137 surface proteins (including 7 isotype controls, refer to Supplementary Table 11) and SARS-CoV-2 S1 protein probe. Then, cells were washed, resuspended in PBS, and counted before proceeding immediately to the single cell partition step.

**b) Single cell CITE-seq library construction and sequencing—**PBMC samples were partitioned into single cell Gel-Bead in Emulsion (GEM) mixed together with the reverse transcription (RT) mix using 10x 5' Chromium Single Cell Immune Profiling Next GEM v2 chemistry (10x Genomics, Pleasanton, CA), as previously described[15]. The RT step was conducted in the Veriti™ Thermal Cycler (ThermoFisher Scientific, Waltham, MA). Single cell gene expression, cell surface protein, T cell receptor (TCR) and B cell receptor (BCR) libraries were prepared as instructed by 10x Genomics user guides (https://www.10xgenomics.com/resources/user-guides/). All libraries were quality controlled using Bioanalyzer (Agilent, Santa Clara, CA) and quantified using Qubit Fluorometric (ThermoFisher). 10x Genomics 5' Single cell gene expression, cell surface protein tag, TCR and BCR libraries were pooled and sequenced on Illumina NovaSeq platform (Illumina, San Diego, CA) using the following sequencing parameters: read1-100-cycle, i7-10-, i5-10, read2-100.

## Serum isolation

Serum was collected directly in Serum Separator Tubes and allowed to clot at room temperature for a minimum of 30 minutes. Within two hours of blood collection, the tubes were spun at 1800 g for 10 minutes at room temperature. The top (serum) layer was removed via pipette and stored in individual vials at −80°C.

## Complete Blood Counts and lymphocyte phenotyping

Subjects had standard complete blood counts with differential (CBCs) performed at the NIH CC in the Department of Laboratory Medicine. Lymphocyte (T cell, B cell, NK cell) flow

cytometry quantification was performed using the BD FACSCanto™ II flow cytometer (BD Biosciences, Franklin Lakes, NJ).

## PBMC in vitro stimulation

PBMCs were thawed and cultured in PRMI1640 containing 10% fetal bovine serum, 2 mM glutamine, 0.055 mM beta-mercaptoethanol, 1% penicillin/streptomycin, 1 mM sodium pyruvate, 10 mM HEPES, and 1% non-essential amino acids and stimulated with the following conditions: 1) IL-15 (10ng/mL), IL-12 (20ng/mL), IL-18 (20ng/mL) for 48 hours; 2) IL-15 (50ng/mL) for 48 hours; 3) IL-18 (50ng/mL) for 48 hours; 4) IL-12 (20ng/mL0, IL-18 (20ng/mL) for 48 hours; 5) anti-CD3 (1ug/mL), anti-CD28 (1ug/mL) for 24 hours; 6) non-stimulated controls. Protein Transport Inhibitor (BD Biosciences cat# 554724) and Brefeldin A (BFA, Invitrogen, cat# 00-4506-51) were added 4 hours before harvest. Cytokines were purchased from BioLegend: IL-15 (cat# 570304), IL-12 (cat# 573004), IL-18 (cat# 592104).

## Flow cytometry

**a) B cell phenotyping panel including influenza HA probes—**Thawed PBMC were washed in RPMI culture medium containing 50U/ml benzonase nuclease and then washed by PBS. Cells were incubated with LIVE/DEAD Fixable Blue Dye (Life Technologies, Carlsbad, CA), which was used to exclude dead cells from analysis. Cells were incubated with fluorochrome-conjugated HAs for influenza B (B/Washington/02/2019 and B/Phuket/3073/2013 combined on the same fluorochrome), and Influenza A H1 (A/Hawaii/70/2019) and H3 (A/Hongkong/2671/2019) and fluorochrome-conjugated antibodies against IgM, IgA, CD21, CD85J, FCRL5, CD20, IgG, CD38, CD14, CD56, CD3, CD27, CD71, CD19, IgD for 30 min at 4 C in the dark. The dyes and detailed information of antibodies in the panel (Sarah Andrews, Vaccine Research Center, National Institute of Allergy and Infectious Diseases, NIH) are summarized in Supplementary Table 12. After incubation with antibodies for 30 minutes, cells were washed two times with FACS buffer (0.1%BSA/PBS (pH7.4)) and fixed in 1% paraformaldehyde. Five million cells were acquired on Cytek Aurora spectral cytometer [Cytek Biosciences, Fremont, CA; SpectroFlo® (Version 2.2.0)]. Data were analyzed with FlowJo software version 10 (BD Biosciences).

**b) General immune phenotyping panel—**Thawed PBMC were washed in RPMI culture medium containing 50U/ml benzonase nuclease and then washed by PBS. Cells were incubated with LIVE/DEAD Fixable Blue Dye (Life Technologies, Carlsbad, CA), which was used to exclude dead cells from analysis. Cells were washed in FACS staining buffer (1 X phosphate-buffered saline, 0.5% fetal calf serum, 0.5% normal mouse serum, and 0.02% $NaN_3$) and incubated with Human Fc block reagent (BD bioscience #564220) at room temperature for 5 min. Cells stained at room temperature for 10 minutes in the dark with fluorochrome-conjugated antibodies against CCR7, CCR6, CXCR5, CXCR3 and TCRgd. Then, stained with fluorochrome-conjugated antibodies against CD45RA, CD16, CD11c, CD56, CD8, CD123, CD161, IgD, CD3, CD20, IgM, IgG, CD28, PD-1, CD141, CD57, CD45, CD25, CD4, CD24, CD95, CD27, CD1c, CD127, HLA-DR, CD38, ICOS, CD21, CD19, CD14 at room temperature for 30 minutes in the dark. Cells were washed two

times with FACS staining buffer (1 X phosphate-buffered saline, 0.5% fetal calf serum, 0.5% normal mouse serum, and 0.02% $NaN_3$) and fixed in 1% paraformaldehyde. Supplementary Table 13 shows the clones and information of antibodies used in the phenotyping panel. A million PBMC were acquired by using Cytek Aurora spectral cytometer [Cytek Biosciences, Fremont, CA; SpectroFlo® (Version 2.2.0)]. The frequency of major populations was analyzed using with FlowJo™ software version 10 (BD Biosciences) based on previously described manual gating strategies[60-62].

**c) In vitro stimulation T cell panel—***In vitro* simulated PBMCs were collected and washed in PBS. Cells were incubated with Zombie UV Fixable Viability Dye (BioLegend) in dark (room temperature) for 20 minutes. Cells were then washed and incubated with Human TruStain FcX (Biolegend) for 10 minutes and subsequently with CCR7 antibody for 10 minutes. Fluorochrome-conjugated antibodies CD8, CD4, HLA-DR, CD69, CD45RA, CD11c, CD5, CDS, TCRVa7.2, CD45RO, CD56, CD122, CD158e/k (KIR3DL1/DL2), KIR2D, NKG2A, CD14, CD29, GPR56 cocktail were added and stained for 30 minutes in dark. Cells were washed and fixed with Fixation/Permeablization (BD Biosciences). Intracellular proteins IFNγ, TNFα, and Ki67 were stained after fixation. Samples were collected using BD FACSymphony flow cytometer (BD Biosciences) and analyzed using FlowJo™ software version 10. Supplementary Table 14 lists the antibodies used in the panel.

## Data processing and transformation

**Bulk RNA-seq data processing—**Sequencing reads from Plate 5 were adaptor- and quality-trimmed to 100 bp using Trimmomatic (v0.38.0)[63] to match the read length of the other plates (resulting reads with less than 100 bp were discarded). Reads were then aligned to the human genome hgS8 using the STAR (v2.6.0b) aligner. Duplicate reads from PCR amplification were removed based on Unique Molecular Identifiers (UMI) using UMI-tools (v0.5.3). Gene expression quantification was performed using the featureCounts[64] function from *Subread* package (v1.6.2). Samples with less than 5 million assigned reads were re-sequenced and replaced. Reads were normalized and log transformed using *limma voom*[65]. Lowly expressed genes, defined as having fewer than five samples with > 0.5 counts per million reads, were removed. Pre-vaccination (days −7 and 0) samples from the same healthy control (HC) subjects were considered as replicates and were used to estimate latent technical factors by the RUVs function from the *RUVSeq*[66] R package (v1.18). Four latent variables were included to derive normalized gene expression values used for visualization and when specifically noted. Variable genes based on intrasubject variability of pre-vaccination samples in the HCs and across technical replicates were filtered out, resulting in a total of 10017 remaining genes for downstream analyses.

### CITE-seq data processing

**a) Single cell sample demultiplexing and preprocessing:** Single cell sequencing data was demultiplexed, converted to FASTQ format, mapped to human hg19 reference genome and counted using *CellRanger* (10x Genomics) pipeline. The sample level demultiplex was done based on two levels as previously described[15]: 1) Hashtag antibody staining to distinguish different timepoint samples from a same subject; 2) single nucleotide polymorphisms (SNPs) called from the whole blood RNA-seq data to identify different

subjects. Specifically, *CellRanger* (v6.0.1) was used for generating count matrix and the software package *demuxlet* (v2, from the *'popscle'* software suite)[67] was used to match single cell gene expression data to each donor and identify empty droplets and doublets.

**b) Single-cell data clustering and cell annotation:** Single-cell data were further processed using Seurat (v4.0.3) running in R v4.1.1. We removed cells with less than 200 and greater than 5,000 detected genes, greater than 60% of reads mapped to a single gene, greater than 15% mitochondrial reads, cell surface protein tag greater than 20,000, and hashtag antibody counts greater than 20,000. The protein data was normalized and denoised using the DSB method (v0.3.0)[68]. The following parameters were used in the dsb normalization function: define.pseudocount = TRUE, pseudocount.use = 10, denoise_counts = TRUE, use.isotype.control = TRUE. The DSB-normalized protein data were used to generate the top variable features (n = 100) and principal components (PCs). Then the shared nearest neighbor (SNN) graph followed by k-nearest neighbors clustering were built using the FindNeighbors and FindClusters functions using first 15 PCs in Seurat (v4.0.3), respectively. Cell clusters were quality controlled based on their nearest neighbors and cell surface proteins. Cells were then further clustered within each major cell population using "weighted-nearest neighbor" (WNN) analysis in Seurat[69] (v4.1.0) by integrating both cell surface protein and gene expression modalities. WNN FindMultiModalNeighbors were done using both top 10 PCs for cell surface protein and RNA of variable features. The WNN clusters were manually annotated and QC using the surface protein together with gene expression.

**c) Effector memory CD8 cell (CD8-EM) annotation for CITE-seq clusters:** All CD8 cells were clustered using WNN as described above. CD8 clusters were annotated based on their surface markers as reported[70] together with gene expression profile. RNA expression of CD8 cells was mapped to external dataset using Seurat Label transfer method[69,71] (v4.1.0). Clusters annotated as CD8-EM are surface CD45ROhi, CD45RAlo, CD95+, CD62Llo and CCR7− (mRNA) with most cells (~90%) mapped to CD8-EM phenotype cells in an external dataset[69,71].

**d) Single cell TCR data processing:** *CellRanger* (v6.0.1) was used to assemble V(D)J contigs. The V(D)J assignment and clonotype were from the CellRanger output of the filtered contig_annotations.csv file for each 10x lane. The data is combined for all lanes and paired TCRα and TCRβ chains for each single cell were combined using *scRepertoire* R package (v1.4.0)[72] and integrated with the single-cell CITE-seq Seurat object metadata. Cells annotated as CD8 T cells and with both α and β chains detected are filtered and analyzed. CD8 subsets and GPR56+ CD8 effector memory cell clonality were visualized with Circos plots using *Circlize* R package (v0.4.14)[73]. For visualization purpose, cells from each subset were downsampled with equal number in each subset (for comparison between subsets, Extended Data Fig. 4g) or in each timepoint (for comparison between timepoints, Extended Data Fig. 4h,i). Cells were considered as the same clone with identical CDR3 (both α and β chains). Identical clones were connected within each sample or each subject across timepoints with lines.

**OLINK serum proteomics—**Missing values were imputed using k-nearest neighbors approach with k=10 using *impute* R package[74] (v1.60.0). For each sample, probes targeting the same protein were averaged.

**Cytek flow cytometry—**Cell frequencies were generated by converting cell counts as fraction of live cells or lymphocytes as specified. The frequency data were log2 transformed for linear modeling. For populations with zero counts in any of the samples, an offset equaling to half of the smallest non-zero value was added across samples.

**CBC with diff and TBNK—**Both absolute and relative counts were log2 transformed for linear modeling. For parameters with zero values in any of the samples, an offset equaling to half of the smallest non-zero value was added across samples.

## Statistical Analysis

**Baseline differential expression analysis—**Using the dream[75] function in the *variancePartition* R package (v1.16.1), mixed-effects models were applied to determine differential levels of analytes (i.e., whole-blood gene expression, serum proteins, cell frequencies, flu titer and SPR, and hematological parameters) between COVID-recovered and HC subjects in a sex-specific manner as follows:

$$\sim 0 + \text{group:sex} + \text{age} + \text{race} + \text{batch.effects} + (1 \mid \text{subject.id})$$

Batch effect-related covariates were added to specific models depending on the assay type. For bulk RNA-seq, these include the four latent technical factors (see Bulk RNA-seq data processing) and the timepoint-matched % neutrophils parameter from the CBC panel. For the Cytek and Olink platforms, sampling batch/plate was included as covariates. In addition to day 0, available samples from day −7 (in RNA-seq and CBC panel), were included as baseline replicates in the modeling.

Sex-specific group differences were computed from the contrasts covid.Female – healthy.Female and covid.Male – healthy.Male. Overall COVID vs. HC difference was determined by combining the two contrasts, i.e. (covid.Female – healthy.Female)/2 + (covid.Male – healthy.Male)/2. Sex difference linked to SARS-CoV2 infection was derived from the contrast (covid.male – covid.female) – (healthy.male – healthy.female) to account for normal differences between males and females. P values were adjusted for multiple testing within each assay type and contrast combination using the Benjamini-Hochberg (BH) method (Benjamini and Hochberg, 1995).

**Association with time since COVID-19 diagnosis—**To evaluate whether any of the differences detected at baseline had stabilized or might still be resolving, a linear model was used to test the association of relevant parameters with the time since COVID-19 diagnosis (TSD) among COVID-recovered subjects:

$$\sim 0 + \text{sex:scale(TSD)} + \text{age} + \text{race} + (1 \mid \text{subject.id})$$

Two asymptomatic subjects without known TSD were excluded from the model. Association assessed separately for females and males, and jointly by the combined contrast (Female:TSD + Male:TSD)/2. Dependent variables were converted to ranks in the model to reduce the effect of potential outliers.

Using a conservative approach, genes were classified as TSD-associated if they had an unadjusted p value < 0.05 and were excluded from subsequent analyses as specified. To determine whether the any of the baseline differential gene sets were associated with TSD, leading edge gene (LEG) modules were derived from the union of all LEGs of the same gene set from different contrasts (see Bulk RNA-seq gene set module scores). A gene set was considered stable if none of three contrasts tested in the association model were significant (using unadjusted p value threshold of 0.05).

**Post-vaccination differential expression analysis—**Similar to the workflow employed in baseline differential expression analysis, mixed-effects models were created to evaluate changes and group differences at each available timepoint after vaccination. Subjects aged 65 and above were excluded as they received a different type of vaccine. In addition to the baseline covariates, the model also accounts for the participants' flu vaccination history within last 10 years as follows:

$$\sim 0 + \text{visit:group:sex} + \text{age} + \text{race} + \text{flu.vax.count.10yr} + \text{batch.effects} + (1 \mid \text{subject.id})$$

Three types of comparisons were examined using this model:

1. Timepoint-specific group differences

   Similar to the contrasts in the baseline model, but for individual timepoints post vaccination (day 1 to day 100).

2. Vaccine-induced changes in group difference

   Similar to the timepoint-specific contrasts above, but additionally subtracting off the corresponding baseline contrast to assess changes relative to the baseline. For example, vaccine-induced changes for female COVID vs. HC differences at D1 is evaluated with the contrast: (D1.covid.Female – D1.healthy.Female) – (Baseline.covid.Female – Baseline.healthy.Female).

3. Reversal of COVID vs. HC difference

   Instead of using the HC subjects at the same corresponding timepoints as reference, postvaccination samples from the COVID-recovered subjects were compared to baseline HC with the contrasts [timepoint].covid.Female – baseline.healthy.Female and [timepoint].covid.Male – baseline.healthy.Male. These contrasts can inform whether any pre-vaccination differences observed in the COVID-recovered subjects were reverted towards healthy baseline levels after vaccination. Reversal is defined as having smaller absolute effect size (using the z.std value from the dream function) at D1 and D28 after vaccination compared to the baseline absolute effect size.

P values were adjusted for multiple testing per each timepoint, assay type and contrast combination using the BH method.

**Gene set enrichment of differentially expressed (DE) genes—**Enriched gene sets were identified using the pre-ranked gene-set enrichment analysis (GSEA) algorithm implemented in the *clusterProfiler* R package (v3.17.0)[76]. Genes were ranked using signed −log10 p values from differential expression models. Enrichment was assessed with gene set lists from MSigDB's Hallmark collection[77], Blood Transcriptomic Modules[78], and cell type gene signatures[79]. Only gene sets with 10 to 300 genes were considered. P values were adjusted per gene set list for each contrast using the BH method and gene sets with FDR < 0.05 were considered significant. Baseline enriched gene sets were derived by intersecting significant gene sets extracted from DE models using samples independently from day −7, day 0, and both days combined. Genes associated with time since diagnosis (TSD) at baseline (see Association with time since COVID-19 diagnosis; Supplementary Tale 1) were excluded from the post-vaccination enrichment analyses to help segregate the effect of vaccination from natural temporal resolution of the SARS-CoV-2 infection.

**Pseudobulk differential expression and gene set enrichment analysis—**Single cells from a given sample were computationally "pooled" according to their cell type assignment by summing all reads for a given gene. Pseudobulk libraries made up by few cells and therefore likely not modeled properly by bulk differential expression methods were removed from analysis for each cell-type to remove samples that contained fewer than 4 cells and less than 35000 library size after pooling. Lowly expressed genes were removed for each cell type individually using the filterByExpr function from *edgeR* (v3.26.8)[80] with min.count = 2. Log counts per million (cpm) of each gene were calculated with scaling factors for library size normalization provided by the calcNormFactors function. Differential expression analysis was performed using the same models described in Post-vaccination differential expression analysis without running baseline models separately because the entire CITE-seq cohort was under 65 years of age. Batch assignment and number of barcodes/cells per sample were included as batch effects in this model.

Similarly, gene set enrichment analysis was carried out for each cell type in the same manner as for the bulk RNA-seq data (see Gene set enrichment of differentially expressed (DE) genes) which particular focus on the baseline enriched genesets identified by the bulk RNA-seq analysis. The Monaco gene sets were excluded from the single-cell analysis given the cell clusters were annotated and no further cell type demultiplex needed.

**Bulk RNA-seq gene set module scores—**Gene set module scores were generated from RUVseq (v1.18) normalized gene expression values (see Bulk RNA-seq data processing and transformation) using gene set variation analysis (GSVA) method in *GSVA* R package (v1.30.0)[81]. LEG module scores representing enriched pathway activities were calculated for relevant samples using LEGs identified by GSEA to enhance signal-to-noise ratio. The average scores between days −7 and 0 were used for calculating post-vaccination changes relative to baseline.

**Pseudobulk gene set module score calculation—**Module scores (gene set signature score) representing enriched pathway activities were calculated for each pseudobulk sample of certain cell types. The pseudobulk gene counts were corrected with removeBatchEffect function in *limma* package (v3.42.2) to remove experimental batch and cell number effects and then normalized with voom[82]. The scores were then generated using gene set variation analysis (GSVA) method from the *GSVA* R package (v1.42.0)[81]. Specifically, for monocyte signatures, LEGs of BTM modules M4.0 and M11.0 were identified by GSEA from 1) D0.COVR-F vs. D0.HC-F and 2) D0.COVR-M vs. D0.HC-M models. The union of LEGs were used for the score calculation for female and male samples, respectively.

For BTM-M7.3 T cell activation signature and other signatures from acute COVID data as indicated in the figures, LEGs were used from the indicated comparison groups for the score calculation of female and male separately.

For monocyte antigen presentation signature, the module score was generated using LEGs from the BTM-M71 enriched in antigen presentation (I) and M95.0 enriched in antigen presentation (II) gene sets of the comparison: D1-D0 change between COVR-M vs. HC-M (Fig. 2f).

For the HALLMARK IFNγ response module score, all genes from the geneset were used for calculation of module scores in each celltype, so that the differences between celltypes can be compared.

**Single-cell module score calculation and visualization—**To visualize the differences between different patient groups in single data of the certain signatures, the genes from indicated genesets were used to calculate the module scores of each single cell. Module scores were calculated using AddModuleScore function in *Seurat (v4.1.0)* and then visualized in UMAP plots. For D1 vs. D0 HALLMARK IFNγ response module score differences shown in umaps, cells from D1.HC-F, D1.COVR-F, D1.HC-M and D1.COVR-M groups were downsampled to the same number of cells. The UMAP embeddings of cells colored with average differences for each high-resolution cell subsets are shown.

**Single-cell module score calculation and test of external acute COVID-19 single-cell CITE-seq data—**Single-cell data from the Brescia cohort of Liu *et al*[15] was downloaded from GEO. Single monocytes data was extracted and Single-cell data from the Brescia cohort were pooled as described in “c) Pseudobulk differential expression and gene set enrichment analysis”. The gene set module scores of BTM modules M4.0 and M11.0 for all samples were generated using the union LEGs of male and female in “d) Gene set module score calculation”. The pseudobulk gene counts were normalized with the varianceStabilizingTransformation function from *DEseq2* R package (v1.34.0)[83]. The scores were then generated using gene set variation analysis (GSVA) method from the *GSVA* R package (v1.42.0)[81]. Given there are multiple samples from each subject, the differences between patient groups (HC, less severe and more severe, corresponding to HC, DSM-low and DSM-high in Liu *et al*) were tested using the *Limma (v3.50.1)* linear model, where samples from the same donors were treated as duplicates using *duplicateCorrelation*. P-values of t statistics from the linear model of indicated contrasts are shown.

**Visualization of gene expression in heatmaps—**Heatmaps showing pseudo-bulk data was generated using *ComplexHeatmap* R package (v2.10.0)[84]. The log(CPM) (counts per million) normalized expression for each sample for a given celltype was calculated by pooling cells as described in "c) Pseudobulk differential expression and gene set enrichment analysis". Heatmaps are showing z-score of the normalized expression for each gene in each sample.

**Data visualization—**Plots were created using ggplot2 (v3.3.5) with ggpubr (v0.4.0) for statistical calculation unless noted.

**Endpoint association—**To evaluate the association of relevant parameters, including gene set module scores and cell frequencies, with interferon (IFN) or antibody titer fold change endpoints, the following model was applied:

$$\text{endpoint} \sim 0 + \text{group:sex} + \text{scale(parameter):group:sex} + \text{age} + \text{race} + \text{flu.vax.count.10yr}$$

The endpoint values were converted to rank to reduce the effects of potential outliers. Replicates from the same subjects were averaged.

**Serology—**Influenza antibody titers below the detection limit of 1:20 were set to 1:10. Maximum titer across strains was calculated by normalizing titer levels across all samples from both day 0 and day 28 individually for each of the four strains followed by taking the maximum standardized titer for each sample.

**Baseline titer difference analysis—**For each of the four strains, a linear model was applied to determine baseline titer differences between COVID-recovered and HC subjects in a sex-specific manner as follows:

$$\text{day 0 titer} \sim \text{group:sex} + \text{age} + \text{race}$$

Titer values were log10 transformed in the model, and sex-specific group differences were computed from the contrasts covid.Female – healthy.Female and covid.Male – healthy.Male. Subjects aged 65 and above were excluded from the analysis.

**Day 28 titer difference analysis—**For post-vaccination titer response, influenza vaccination history and baseline titer were included as covariates to partly account for prior exposure, similar to the approach used for influenza vaccine evaluation by the Food and Drug Administration (e.g., see https://www.fda.gov/media/135687/download page 27). Both day 28 titer and day 28/day 0 fold change (FC) were evaluated as endpoints to determine group differences between COVID-recovered and HC subjects for each of the four strains:

$$\text{endpoint} \sim \text{group:sex} + \text{age} + \text{race} + \text{flu.vax.count.10yr} + \text{day 0 titer}$$

For day 28 FC, a negative binomial model with log link was applied using glm.nb function in the *MASS* R package (v7.3-53). A linear model was used to fit the day 28 titers.

Strain-specific titer values were log10 transformed in the model. Group differences were assessed using the same subjects and contrasts as in the baseline analysis.

Influenza antibody avidity as measured by surface plasmon resonance (SPR) were analyzed in the same manner as the titer data across HA1 and HA2, with the exception that that a linear model was applied for the fold changes.

**Concordance in natural influenza infection cohort—**A prospective cohort study with subjects profiled prior to and at least 21 days after natural influenza infection in two seasons[18] was utilized to assess residual effects of the infection separately in males and females. Gene expression data were downloaded from GEO using the accession GSE68310. Subjects with only influenza A virus infection (n=51 females and 35 males) were identified and included for this analysis. Lowly expressed probes were removed, and the remaining data were converted to gene-based expressions. No additional processing steps were performed as the data were already normalized.

Separately for each season, differential expression analysis between baseline (pre-infection) and spring (long term post-infection) samples from the same individuals were performed using the dream function in the *variancePartition* R package (v1.16.1). A mixed-effects model accounting for flu vaccination history and disease severity (based on fever grade: none, low, and high) was constructed as follows:

$$\sim 0 + \text{timepoint:sex} + \text{age} + \text{num.flu.vaccination} + \text{fever.grade} + (1 \mid \text{subject.id})$$

Differentially expressed (DE) genes were identified using the contrasts Spring.F - Baseline.F and Spring.M – Baseline.M for females and males, respectively. Sex difference was evaluated by the contrast (Spring.M – Baseline.M) – (Spring.F - Baseline.F). Concordance of DE results between the two seasons were evaluated based on correlation of effect size across genes (z.std values generated by dream).

Enrichment analysis was performed to determine whether the same set of genes were differentially expressed between pre- and post-influenza infection from this independent cohort and in COVID-recovered subjects compared to healthy controls prior to vaccination. To better match the age range of subjects between the two studies, baseline differential gene analysis was performed again with subjects under 65 years of age in the COVID cohort (see Baseline differential expression analysis). Given that the males showed stronger concordance between the two flu seasons (Extended Data Fig. 2b), COVID DE genes were ranked by signed −log10 p values and tested against a gene set formed by the intersect of DE ($p < 0.05$) genes in males from the flu infection cohort.

**Elastic Net Multivariate Predictive Modeling—**Elastic net models were constructed using the *eNetXplorer* R package (v1.1.3)[85] to predict day 1 (D1) INF$\gamma$ response after influenza vaccination with both CITE-seq and flow cytometry cell frequencies at D0 as predictors. A total of 33 subjects (COVR-F=11, HC-F=8, COVR-M=9, HC-M=5) with both CITE-seq and flow cytometry data were included. Based on 20 runs of 5-fold cross validation, a grid of regularization parameters ($\alpha$ and $\lambda$) were tested to determine models

with best performance and cell subsets with consistent predictive power. Model performance was assessed by the mean squared error between the predicted and observed response. Importance of a cell population was determined by the frequency it was selected by the models (i.e., having non-zero coefficient). P values of the model performance and feature importance were derived by comparing to null models constructed with permuted response.

**TCR diversity metric calculation—**Shannon's entropy (H' index) was calculated as a measure of TCR diversity[86,87]. Samples for each CD8 subsets with fewer than 50 cells were filtered from the calculation. All samples were downsampled to 50 cells because the diversity metric can be affected by the sample cell numbers. The process was repeated 1000 times with random downsampling of 50 cells and the median Shannon's index was used as an estimate of diversity for a given sample. Differences of the diversity metric between different CD8 subsets or timepoints were tested using two-tailed Wilcoxon test.

**Reversal genes and bootstrapping to infer significance of difference in reversal of monocyte repressed signature between COVR-F and COVR-M—** Reversal genes are defined as those whose COVR vs. D0 HC absolute effect size (z.std values from dream; see Post-vaccination differential expression analysis) are smaller at both D1 and D28 compared to D0.

Bootstrapping was employed to determine the significance of difference between COVR-F and COVR-M in their proportion of baseline LEGs from the monocyte depressed signature (BTM M4.0 and M11.0) that moved towards baseline HC. Subjects from each subject group were randomly sampled with replacement in each round of the bootstrapping and their samples were analyzed as described in Post-vaccination differential expression analysis. The proportion of LEGs reversed after vaccination were calculated in each round for COVR-F and COVR-M in classical and non-classical monocytes, separately, and the p values plotted in Fig. 4e were determined based on 20 rounds of this procedure.

## Extended Data

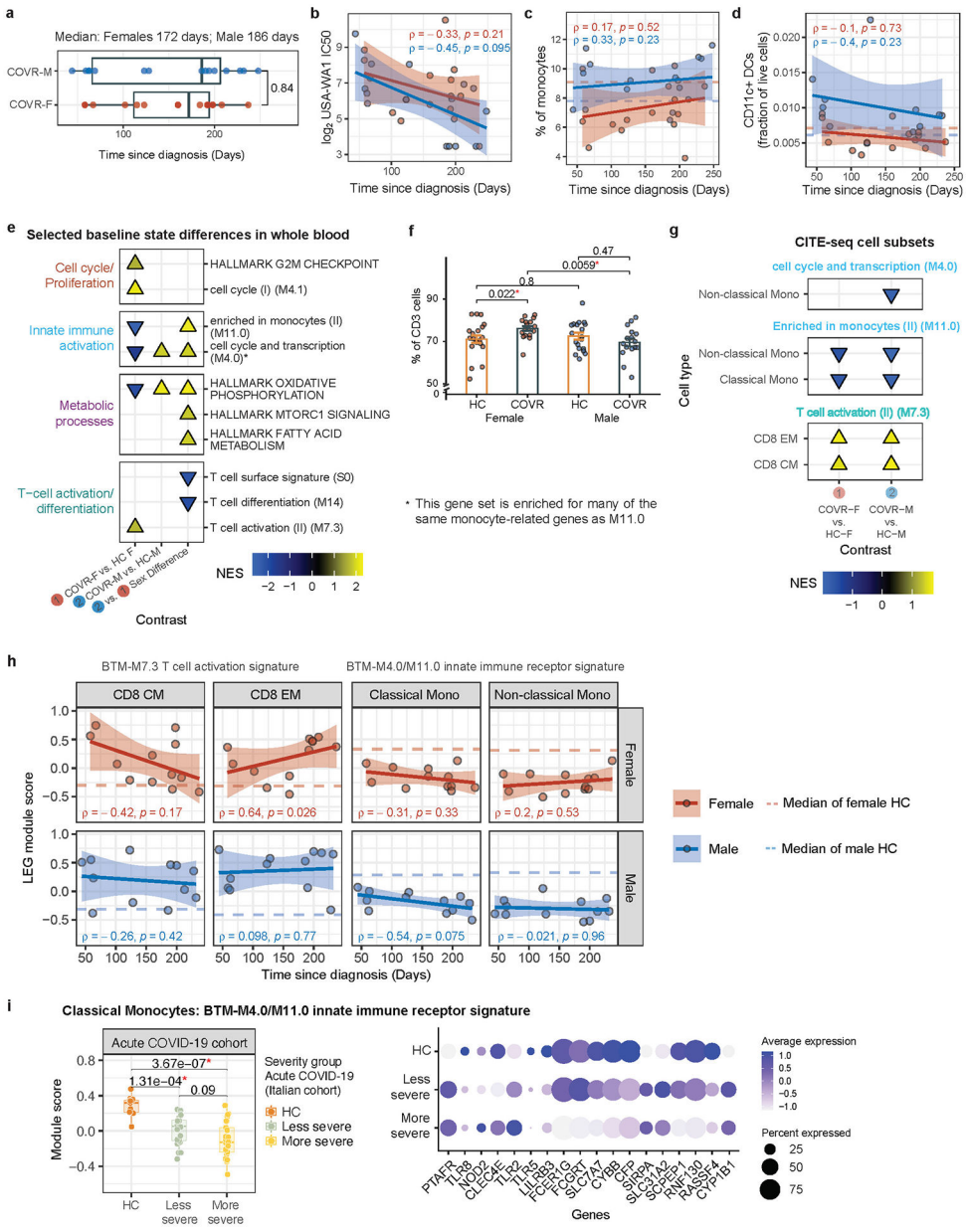


**Extended Data Figure 1. Baseline differences between COVID-19-recovered subjects and matching controls.**

**a**, Box plot showing the distribution of time since diagnosis (TSD; x-axis) in COVR-F (n=16) and COVR-M (n=15). Two participants with asymptomatic COVID-19 infection and thus unknown TSD are not included. Significance of group difference is determined by two-tailed Wilcoxon test.

**b**, Scatterplot showing the correlation between the TSD (x-axis) and the SARS-CoV-2 neutralization titer (WA1 strain; y-axis) for COVR subjects at D0 prior to influenza vaccination. Spearman's rank correlation and unadjusted p values are shown. Participants

with asymptomatic COVID-19 infection not included in TSD analyses. The shaded area represents 95% confidence interval.

**c**, Similar to (**b**), but for the percentage of monocytes in peripheral blood as measured by the complete blood count (y-axis) at D0. Dotted lines represent median level in HC-F and HC-M.

**d**, Similar to (**b**), but for the proportion of CD11c+ dendritic cells (DCs; as fraction of live cells; y-axis) as measured by flow cytometry of PBMCs at D0.

**e**, Blood transcriptomic analysis of the stable baseline (pre-vaccination) differences among COVR and HC groups. Enrichment plot shows the normalized enrichment scores (NES) of selected gene sets of the different comparisons (GSEA FDR < 0.05; see Methods; see Supplementary Table 3 for all significant gene sets with FDR < 0.05). The NES are plotted separately for COVR-F versus HC females (HC-F), COVR-M versus HC males (HC-M), or the difference between the two sets of comparisons (COVR-M versus COVR-F taking healthy sex differences into account). Positive (negative) NES indicates that gene set scores are higher (lower) in the first group than the second group listed in the comparison. Only gene sets not correlated with TSD across COVR subjects at baseline are considered stable.

**f**, Similar to Fig. 1d, but for percent of CD3+ cells (T cells).

**g**, Similar to (**e**), but for a subset of monocyte and T-cell activation gene sets with significant enrichment ($p < 0.05$) using the D0 CITE-seq pseudobulk expression for the specified cell types (see Methods; see Supplementary Table 5 for complete results).

**h**, Scatterplots showing the relationship between the TSD and leading-edge gene (LEG) module scores [left two boxes: the T-cell activation gene set (BTM-M7.3); right two boxes: the union of the LEGs from gene sets BTM M4.0 and M11.0; see Methods] in COVR-F (n=12) (top row) and COVR-M (n=12) (bottom row) at D0 using the CITE-seq pseudobulk data of the indicated cell types. Each dot represents a COVR subject. The dotted lines represent the median score for the sex-matched HC group at D0 in the comparison shown. Spearman's rank correlation and p values are shown. The shaded area represents 95% confidence interval.

**i**, (left) Box plot comparing the classical monocyte pseudobulk module scores of the LEGs used in Fig. 1f (union of female (F) and male (M) gene sets) in an acute COVID-19 CITE-seq dataset from Liu *et al*[15]. Both M (n=50) and F (n=9) subjects are included in all three groups (HC n=13, less severe n=21, more severe n=25). Each dot represents a sample. Unadjusted p values from the indicated two-group comparisons are shown. P values were generated using the moderated T statistics from a linear model in which samples from the same donors were treated as duplicates (See Methods). (right) Bubble plot showing expression of the genes in Fig. 1f right panel within the classical monocyte CITE-seq data from Liu *et al.* in the same three patient groups shown in the left panel. All box plot elements are the same as indicated in Fig. 1.

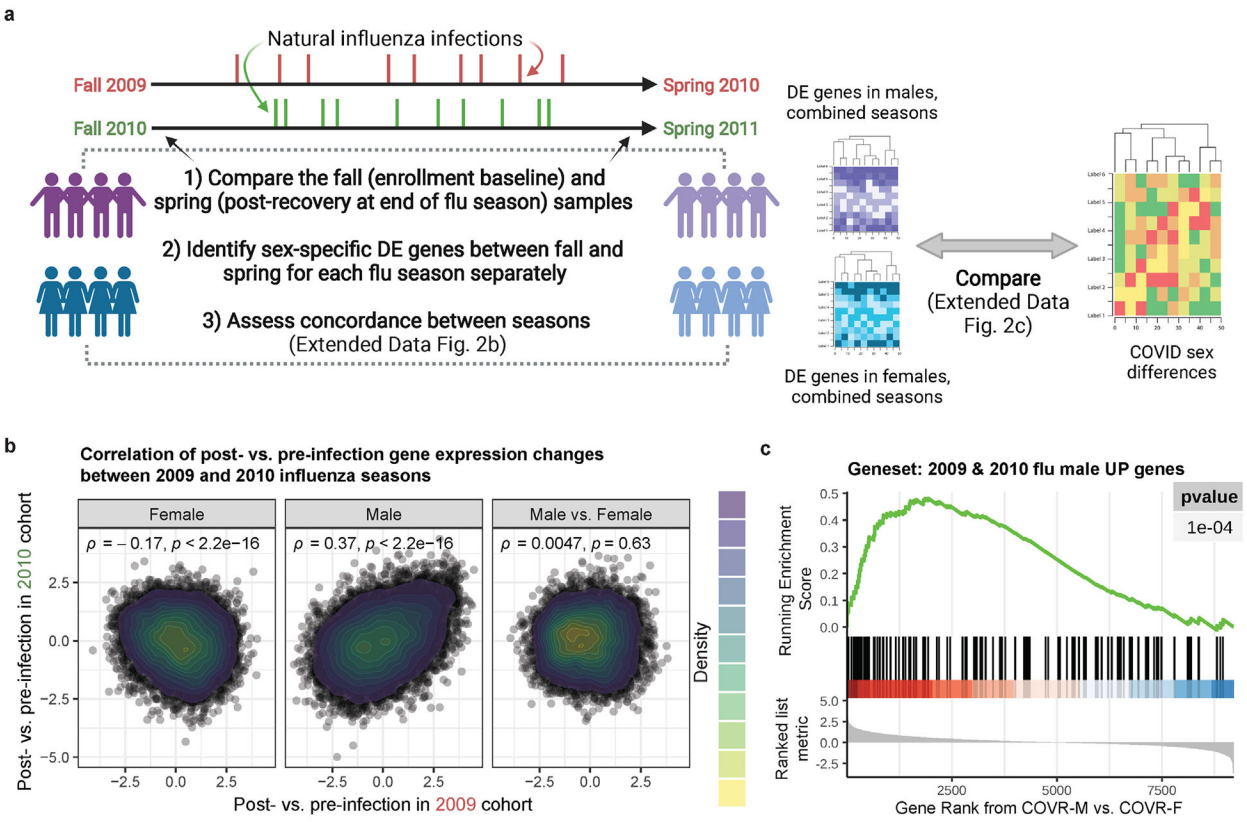


**Extended Data Figure 2. Persistent post-infection gene expression changes following natural influenza infection.**

**a**, Schematic showing the approach used to evaluate changes in blood gene expression between before (pre-infection baseline) and months after natural influenza infection over two distinct seasons published in Zhai *et al*[18], and how those gene changes may relate to sex-specific differences resulted from prior COVID-19 in this study.

**b**, Scatter density plot showing the correlation between the gene expression changes (see Extended Data Table 7) before (fall) and after (spring) natural influenza A infection in 2009 (x-axis) and 2010 (y-axis) for females (F; left), males (M; center), and M vs F contrast (right). Shown are Spearman's rank correlation and unadjusted p values.

**c**, Gene set enrichment plot of the genes that increased in M between fall (pre-infection) and spring (post-infection) in both 2009 – 2010 and 2010 – 2011 seasons. Genes were ranked by the signed log10(unadjusted p-value) in the COVID-19-recovered (COVR)-M vs COVR-F contrast at baseline using only subjects under 65 years of age. The tick marks denote the location of the genes in the influenza gene set.

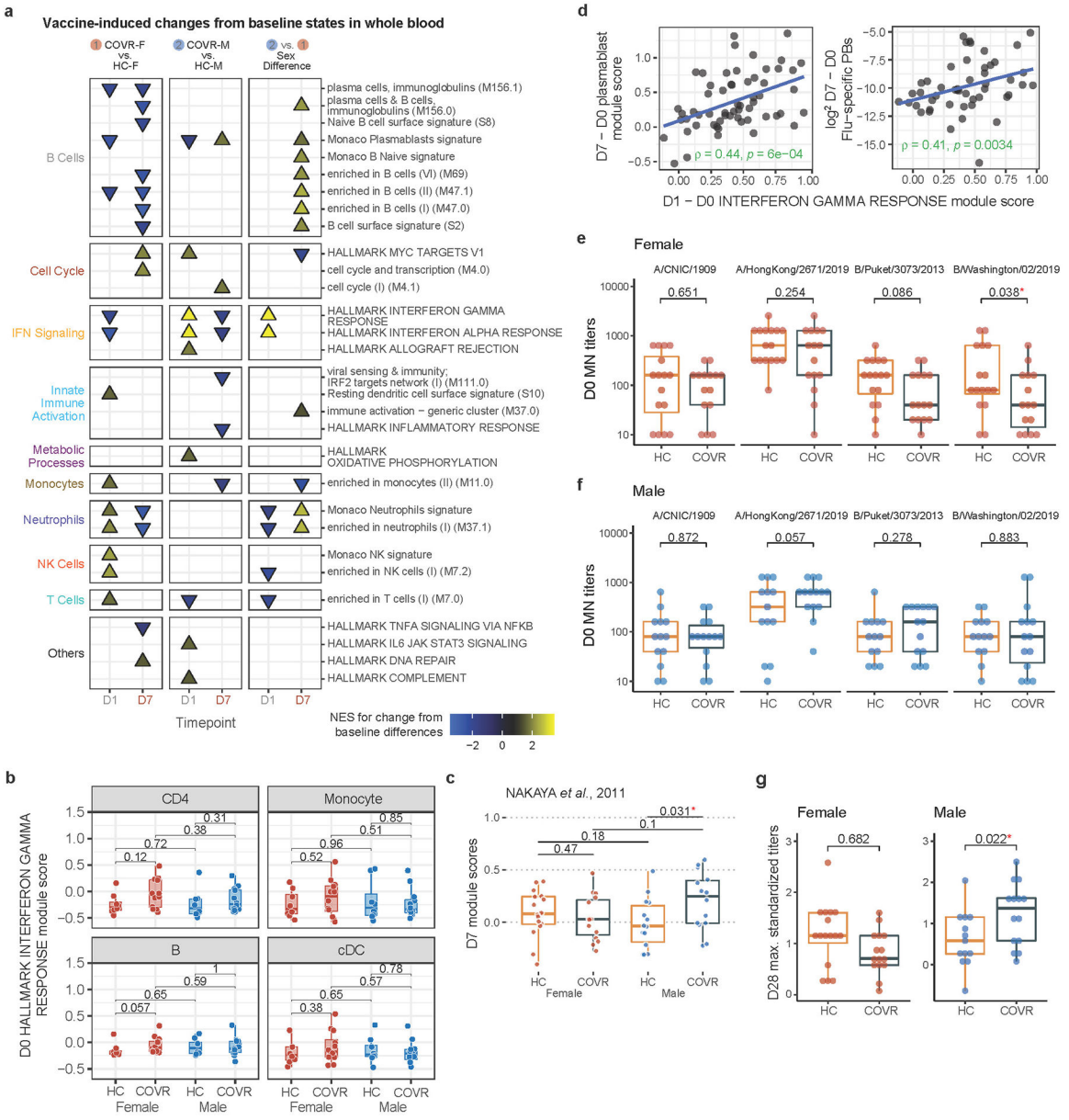


**Extended Data Figure 3. Sex-specific molecular, cellular, and humoral response differences to influenza vaccination in COVID-19-recovered individuals and matching controls.**

**a**, Similar to Extended Data Fig. 1e but here showing enriched gene sets in whole blood comparing the early [day 1 (D1) and day 7 (D7)] influenza vaccination responses in COVID recovered (COVR) vs. healthy control (HC) subjects for females (F; Contrast 1), males (M; Contrast 2), and sex differences (Contrast 2 vs. 1; i.e., COVR-M versus COVR-F taking healthy sex differences into account; see Methods). Plotted are the gene sets that show significant changes from the baseline [day −7 and day 0 (D0)] within each comparison group [e.g., COVR-F and HC-F for D1] and significant differences between the two groups at the indicated timepoints (FDR < 0.05; see Supplementary Table 5).

**b**, Similar to Fig. 2e, but showing the D0 Hallmark IFNγ Response module score for the indicated cell types from the CITE-seq pseudobulk expression data. CD4 = CD4+ T-cells; cDC = conventional/myeloid dendritic cells; B = B-cells.

**c**, Box plot showing the D7 whole blood signature score from genes identified in Nakaya *et al*[88] whose D7/D0 fold-change positively correlated with day 28 (D28) influenza hemagglutination inhibition titers. Only subjects under 65 years of age [COVR-F (n=15), COVR-M (n=14), and HC-F (n=16), and HC-M (n=14)] are included. Significance of differences is determined by two-tailed Wilcoxon test.

**d**, Scatter plot showing the correlation of the whole blood D1 – D0 Hallmark Interferon Gamma Response gene set module score (x-axis) to the whole blood D7 – D0 plasmablast (PB) gene set module score (left y-axis; Monaco *et al*[79]) and D7 – D0 difference of influenza-specific PB (all HA+ CD27+ CD38+ $CD20^{low}$ $CD21^{low}$) frequency from flow cytometry (right y-axis; as fraction of CD19+ B-cells). Only study participants < 65 years of age are included. Spearman's rank correlation and unadjusted p values are shown.

**e**, Box plots showing the D0 (pre-vaccination) microneutralization titers for each of the four strains in the seasonal influenza vaccine (columns) in females (COVR-F and HC-F) under the age of 65. Unadjusted p values are from linear models accounting for age and race (see Methods).

**f**, Similar to (**e**) but for males (COVR-M and HC-M) under 65 years of age.

**g**, Maximum standardized influenza vaccine titer (among the four strains in the vaccine) at D28 after vaccination for females (left) and males (right), respectively. Unadjusted p values are from linear regression models accounting for age, race, influenza vaccination history, and baseline influenza titer (see Methods). Unadjusted p values are shown. All box plot elements are the same as indicated in Fig. 2.

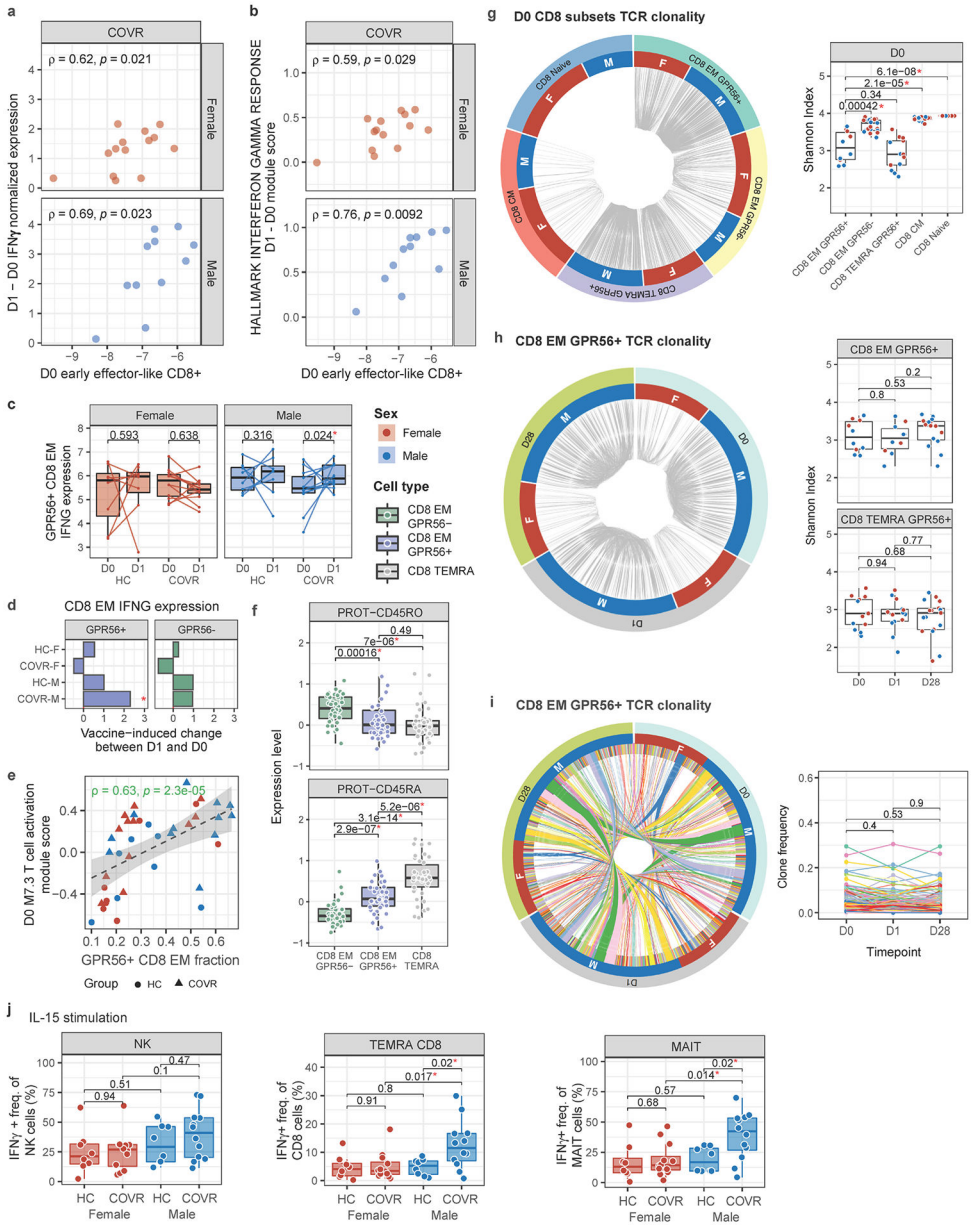

**Extended Data Figure 4. GPR56+ virtual memory-like CD8+ T-cells contribute to increased day 1 IFNγ response in COVID-19-recovered males.**

**a**, Scatterplots showing the correlation between the day 0 (D0) $\log_2$ frequency of early effector-like CD8+ T-cells measured by flow cytometry (as fractions of live lymphocytes; see Population 50 in Supplementary Table 9 and Supplementary Fig. 1; x-axis) and the change (D1 – D0) in serum interferon gamma (IFNγ) protein levels measured by the OLINK platform (y-axis) for COVID-19-recovered (COVR) females (COVR-F; top, n=14) and COVR males (COVR-M; bottom; n=11). Spearman's rank correlation and p values are shown.

**b**, Similar to (**a**) but showing the correlation between the D0 $\log_2$ frequency of early effector-like CD8+ T-cells measured by from flow cytometry (as fraction of live

lymphocytes; x-axis) and the change (D1 - D0) in the whole blood signature score of the Hallmark IFNγ Response gene set (y-axis).

**c,** Box plots comparing D0 and D1 pseudobulk IFNG gene expression (y-axis) in GPR56+ CD8 EM population for HC-F (n=8), COVR-F (n=12), HC-M (n=8) and COVR-M (n=12). Significance is determined by a linear model accounting for age, race, and influenza vaccination history (see Methods).

**d**, Bar plot showing the T statistic of the vaccine-induced change (D1 - D0) in IFNγ gene (IFNG) expression using CITE-seq pseudobulk data (x-axis) within the GPR56+ and GRP56− CD8 EM for HC-F (n=8), COVR-F (n=12), HC-M (n=8), and COVR-M (n=12). * $p < 0.05$ with exact value shown in **(c)**.

**e**, Scatter plot showing the correlation between GPR56+ CD8 EM cell frequency (as fractions of total CD8 EM in the CITE-seq data; x-axis) and BTM-M7.3 T-cell activation signature score of CD8 EM cells computed using CITE-seq pseudobulk gene expression data (y-axis). Spearman correlation and p values are shown. The shaded area represents the 95% confidence interval.

**f**, Related to Fig. 3h but showing CD45RA and CD45RO only with CD8+ TEMRA cells included as an additional comparator.

**g**, (left) Circos plot of T-cell receptor (TCR) clonality for different CD8+ T-cell subsets at D0. Segments in the outer circle represent different CD8+ T-cell populations. Segments in inner circle represent male (M) and female (F) for both COVR and HC subjects. Grey lines connect clones sharing identical CDR3 sequences within each individual. Cell subsets are downsampled for visualization (see Methods). (right) Box plot showing Shannon's entropy index (y-axis) at D0 for each of the indicated CD8+ populations. Significance of differences is determined by two-tailed Wilcoxon test. Shannon's entropy index evaluates the TCR repertoire diversity for each sample. Higher indices indicate higher diversity (i.e., fewer shared clones shown in Circos plot). EM = effector memory; CM = central memory; TEMRA = EM cells re-expressing CD45RA.

**h**, (left) Circos plot of TCR clonality for GPR56+ CD8 EM cells at different timepoints. Segments in the outer circle represent different days in the study (D0, D1, D28). Segments in the inner circle represent males (M) and females (F) for both COVR and HC subjects. Grey lines connect clones sharing identical CDR3 sequences within each sample. Timepoints are downsampled for visualization purposes (see Methods). (right) Box plot showing Shannon's entropy index (y-axis) of TCR clonality at each of the indicated time points (D0, D1, D28; x-axis) for GPR56+ CD8 EM T-cells (left) and GPR56+ CD8+ TEMRA (right). Significance of differences is determined by two-tailed Wilcoxon test.

**i**, (left) Similar to (**h**), but showing the shared clones among different timepoints (segments in the outer circle). Segments in the inner circle represent unique clones for each individual. Clones and lines connecting shared clones are colored. Samples with less than 30 cells were filtered out for visualization purposes. (right) Line chart showing frequencies of each clone (y-axis) shown in Circos plot (left) at D0, D1 and D28 for each subject. P-values of paired Wilcoxon test are shown comparing the clone frequency differences among D0, D1 and D28.

**j,** Related to Fig. 3i but showing the frequencies of IFNγ$^+$ NK, IFNγ$^+$ CD45RA+ CD45RO+ TEMRA CD8+ T-cells and IFNγ+ MAIT cells after IL-15 stimulation *in vitro*. All box plot elements are the same as indicated in Fig. 3. Unadjusted p values are shown.

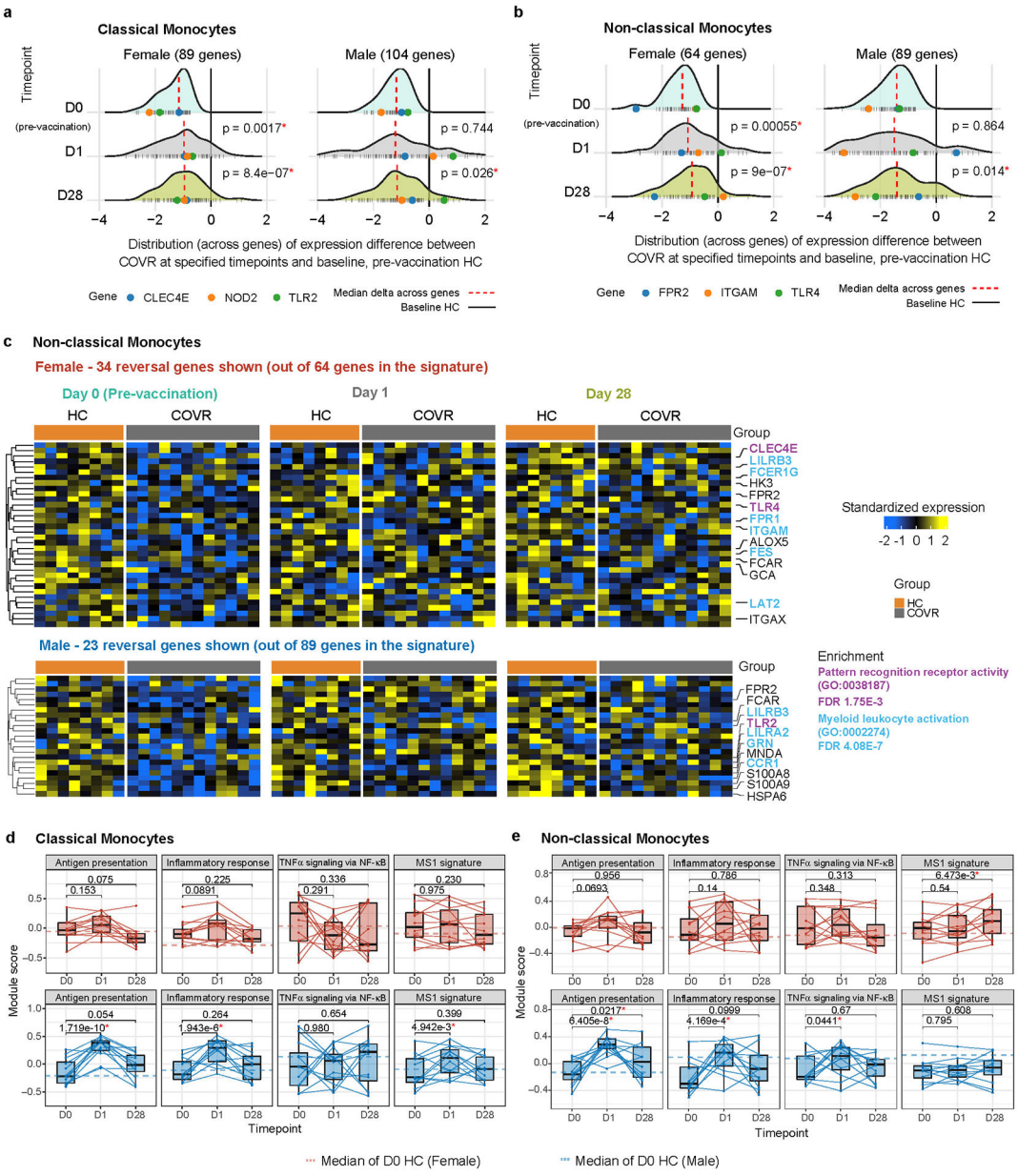


**Extended Data Figure 5. Changes in immune states in COVID-19-recovered individuals following influenza vaccination.**

**a**, Distributions of gene-level difference of the innate immune receptor (IIR) signature (see Fig. 1f) in classical monocytes separately for females (F) and males (M) [shown as z-scores, on a per gene level, capturing the average difference between COVID Recovered (COVR) at the indicated timepoint (top to bottom: D0, D1, and D28) and healthy control (HC) at D0; see Methods]. Dashed red vertical lines represent the median of the distribution. Dark tick marks at the bottom represent individual genes and colored dots highlight specific genes of interest. Significance of differences from D0 is determined by paired two-tailed Wilcoxon test.

**b**, Similar to (**a**) but for the non-classical monocytes (see Fig. 1g).

**c**, Similar to Fig. 4d but for non-classical monocytes (see Fig. 1g for the innate receptor signature in non-classical monocytes).
**d**, Similar to Fig. 4b but for COVR-F (red) and COVR-M (blue) only and gene sets shown on top of each plot. Box plots showing the classical monocyte LEG module scores (y-axis) of gene sets from Supplementary Fig. 2: antigen presentation related gene sets, Hallmark Inflammatory response, Hallmark TNF-α signaling via NF-κB, and MS-1 signature from Reyes *et al*[17]. LEGs from the first three gene sets were found to be repressed in acute COVID-19 patients in Liu *et al*[15].
**e**, Similar to (**d**), but for non-classical monocytes. All box plot elements are the same as indicated in Fig. 4. Unadjusted p values are shown.

## Extended Data Table 1.
## Cohort characteristics.

Demographics (age, sex, self-reported race), influenza vaccination history, and COVID-19 related information (for recoverees). COVR = COVID-19 recovered.

| | COVR | | Healthy | |
|---|---|---|---|---|
| | **Female** | **Male** | **Female** | **Male** |
| Subject count | 17 | 16 | 21 | 19 |
| **Age (Years)** | | | | |
| Median | 40.2 | 43.7 | 52.5 | 47.6 |
| Mean | 44.9 | 43.7 | 47.2 | 47.4 |
| Min | 23.4 | 21.9 | 22.5 | 24.0 |
| Max | 70.5 | 67.3 | 70.4 | 69.1 |
| Aged > 65 | 2 | 2 | 5 | 5 |
| **Race** | | | | |
| Asian | 1 | 0 | 2 | 2 |
| Black | 1 | 0 | 4 | 0 |
| Multiple races | 0 | 2 | 1 | 3 |
| White | 15 | 14 | 14 | 14 |
| **Number of Influenza Vaccination in Past 10 Years** | | | | |
| 0 | 0 (0%) | 1 (6.25%) | 0 (0%) | 2 (10.53%) |
| 1 | 1 (5.88%) | 0 (0%) | 1 (4.76%) | 0 (0%) |
| 2 | 0 (0%) | 1 (6.25%) | 2 (9.52%) | 2 (10.53%) |
| 3 | 1 (5.88%) | 0 (0%) | 1 (4.76%) | 0 (0%) |
| 4 | 0 (0%) | 0 (0%) | 2 (9.52%) | 0 (0%) |
| 5 | 3 (17.65%) | 3 (18.75%) | 1 (4.76%) | 0 (0%) |
| 6 | 1 (5.88%) | 1 (6.25%) | 1 (4.76%) | 0 (0%) |
| 7 | 3 (17.65%) | 0 (0%) | 1 (4.76%) | 1 (5.26%) |
| 8 | 0 (0%) | 1 (6.25%) | 1 (4.76%) | 3 (15.79%) |
| 9 | 1 (5.88%) | 1 (6.25%) | 1 (4.76%) | 1 (5.26%) |
| 10 | 7 (41.18%) | 8 (50%) | 10 (47.62%) | 10 (52.63%) |
| Experienced side effects after vaccination | 16 (94.1%) | 9 (56.3%) | 17 (90.0%) | 15 (78.9%) |
| **COVID-19 Symptoms** | | | | |

| | COVR | | Healthy | |
|---|---|---|---|---|
| | Female | Male | Female | Male |
| Asymptomatic | 1 (5.9%) | 1 (6.3%) | - | - |
| Symptomatic | 16 (94.1%) | 15 (93.8%) | | |
| **Time since COVID-19 Diagnosis (Days)** * | | | | |
| Median | 172.0 | 186.0 | - | - |
| Mean | 152.9 | 149.3 | - | - |
| Min | 58.0 | 44.0 | - | - |
| Max | 237.0 | 248.0 | - | - |
| **Duration of acute COVID-19 symptoms (Days)** * | | | | |
| Median | 14 | 11 | | |
| Mean | 19.62 | 22.07 | | |
| Min | 4 | 1 | | |
| Max | 87 | 140 | | |
| Experienced COVID-19 residual symptoms at time of screening | 8 (47.1%) | 3 (18.8%) | - | - |
| **COVID-19 Residual Symptoms** | | | | |
| Brain fog | 1 (5.9%) | 0 (0%) | - | - |
| Fatigue | 2 (11.8%) | 0 (0%) | - | - |
| Loose stools | 0 (0%) | 1 (6.3%) | - | - |
| Reduced sense of taste | 1 (5.9%) | 1 (6.3%) | - | - |
| Reduced sense of smell / smell disturbances | 5 (29.4%) | 2 (12.5%) | - | - |
| Shortness of breath / Chest pressure | 1 (5.9%) | 0 (0%) | - | - |

* Excluding asymptomatic subjects

## Supplementary Material

Refer to Web version on PubMed Central for supplementary material.

## Acknowledgements

We are indebted to the study participants whose generosity has expanded our scientific understanding of COVID-19 and viral infections in general. We thank Kaitlyn Sadtler for assistance with the development of the Cytek 36-color flow cytometry panel, Qin Xu for assistance with the design of the cytokine stimulation experiments, Foo Cheung for computational assistance, Matthew Mulé for providing software ("dsb"), the NCI CCR Sequencing Facility for sequencing support, NIAID HPC Team for computing support, and Ronald Germain for critical reading of the manuscript. Fig. 1a, 1b, 2a, 3a, 4a, Extended Data Fig. 2a were created using BioRender.com. This research was supported by the Intramural Research Programs of the NIAID and the Intramural Programs of the NIH Institutes supporting the NIH Center for Human Immunology. JH was funded in part with federal funds from the National Cancer Institute, National Institutes of Health, under Contract No. 75N91019D00024. The content of this publication does not necessarily reflect the views or policies of the Department of Health and Human Services, nor does mention of trade names, commercial products, or organizations imply endorsement by the U.S. Government.

## Data Availability

Raw and processed data from the whole blood bulk RNA-seq and single-cell CITE-seq are available from the NCBI Gene Expression Omnibus, accession numbers GEO: GSE194378 (https://www.ncbi.nlm.nih.gov/geo/query/acc.cgi?acc=GSE194378) and GEO:GSE206265 (https://www.ncbi.nlm.nih.gov/geo/query/acc.cgi?acc=GSE206265). respectively. Additional

datasets, including clinical, proteomics, flow cytometry, and influenza antibody measurements, are available at: https://doi.org/10.5281/zenodo.5935845. The influenza infection dataset we utilized was downloaded directly from GEO: GSE68310 (https://www.ncbi.nlm.nih.gov/geo/query/acc.cgi?acc=GSE68310). Reprint requests, permissions, and requests for materials may be directed to the corresponding author, John Tsang (john.tsang@yale.edu).

## Code Availability

Analysis code, extended patient and sample metadata are available at: https://github.com/niaid/covid-flu.

## Consortia authors

OP11 Clinical Staff: Princess Barber[11], Daly Cantave[11], Anne Carmona[11], Jean Hammer[12], Alaina K. Magnani[11], Valerie Mohammed[11], Cindy Palmer[11], Deitra Shipman[11]

11 Clinical Center Nursing Department, NIH, Bethesda, MD, USA

12 Clinical Research Directorate, Frederick National Laboratory for Cancer Research, Frederick, MD, USA

## Main Text References

1. Mina MJ et al. Measles virus infection diminishes preexisting antibodies that offer protection from other pathogens. Science 366, 599–606 (2019). [PubMed: 31672891]
2. Tomalka JA, Suthar MS, Diamond MS & Sekaly RP Innate antiviral immunity: how prior exposures can guide future responses. Trends Immunol. 43, 696–705 (2022). [PubMed: 35907675]
3. Tsang JS et al. Improving Vaccine-Induced Immunity: Can Baseline Predict Outcome? Trends Immunol. 41, 457–465 (2020). [PubMed: 32340868]
4. Goodridge HS et al. Harnessing the beneficial heterologous effects of vaccination. Nat. Rev. Immunol 16, 392–400 (2016). [PubMed: 27157064]
5. Aaby P, Netea MG & Benn CS Beneficial non-specific effects of live vaccines against COVID-19 and other unrelated infections. Lancet Infect. Dis S1473-3099(22)00498-4 (2022) doi:10.1016/S1473-3099(22)00498-4.
6. Netea MG et al. Defining trained immunity and its role in health and disease. Nat. Rev. Immunol 20, 375–388 (2020). [PubMed: 32132681]
7. Nalbandian A. et al. Post-acute COVID-19 syndrome. Nat. Med 27, 601–615 (2021). [PubMed: 33753937]
8. Olsen SJ et al. Changes in Influenza and Other Respiratory Virus Activity During the COVID-19 Pandemic - United States, 2020-2021. MMWR Morb. Mortal. Wkly. Rep 70, 1013–1019 (2021). [PubMed: 34292924]
9. Sudre CH et al. Attributes and predictors of long COVID. Nat. Med 27, 626–631 (2021). [PubMed: 33692530]
10. Stoeckius M. et al. Simultaneous epitope and transcriptome measurement in single cells. Nat. Methods 14, 865–868 (2017). [PubMed: 28759029]
11. Ursin RL & Klein SL Sex Differences in Respiratory Viral Pathogenesis and Treatments. Annu. Rev. Virol 8, 393–414 (2021). [PubMed: 34081540]
12. Wheatley AK et al. Evolution of immune responses to SARS-CoV-2 in mild-moderate COVID-19. Nat. Commun 12, 1162 (2021). [PubMed: 33608522]

13. Schultze JL & Aschenbrenner AC COVID-19 and the human innate immune system. Cell 184, 1671–1692 (2021). [PubMed: 33743212]
14. Sette A & Crotty S Adaptive immunity to SARS-CoV-2 and COVID-19. Cell 184, 861–880 (2021). [PubMed: 33497610]
15. Liu C et al. Time-resolved systems immunology reveals a late juncture linked to fatal COVID-19. Cell 184, 1836–1857.e22 (2021). [PubMed: 33713619]
16. Paludan SR & Mogensen TH Innate immunological pathways in COVID-19 pathogenesis. Sci. Immunol (2022) doi:10.1126/sciimmunol.abm5505.
17. Reyes M. et al. Plasma from patients with bacterial sepsis or severe COVID-19 induces suppressive myeloid cell production from hematopoietic progenitors in vitro. Sci. Transl. Med (2021) doi:10.1126/scitranslmed.abe9599.
18. Zhai Y. et al. Host Transcriptional Response to Influenza and Other Acute Respiratory Viral Infections – A Prospective Cohort Study. PLOS Pathog. 11, e1004869 (2015). [PubMed: 26070066]
19. Pulendran B. Systems vaccinology: Probing humanity's diverse immune systems with vaccines. Proc. Natl. Acad. Sci 111, 12300–12306 (2014). [PubMed: 25136102]
20. Tsang JS Utilizing population variation, vaccination, and systems biology to study human immunology. Trends Immunol. 36, 479–493 (2015). [PubMed: 26187853]
21. Pulendran B, Arunachalam PS, & O'Hagan DT Emerging concepts in the science of vaccine adjuvants. Nat. Rev. Drug Discov 20, 454–475 (2021). [PubMed: 33824489]
22. Bucasas KL et al. Early Patterns of Gene Expression Correlate With the Humoral Immune Response to Influenza Vaccination in Humans. J. Infect. Dis 203, 921–929 (2011). [PubMed: 21357945]
23. Auladell M. et al. Influenza virus infection history shapes antibody responses to influenza vaccination. Nat. Med 28, 363–372 (2022). [PubMed: 35177857]
24. Truong K-L et al. Killer-like receptors and GPR56 progressive expression defines cytokine production of human CD4+ memory T cells. Nat. Commun 10, 2263 (2019). [PubMed: 31118448]
25. Nicolet BP et al. CD29 identifies IFN-γ–producing human CD8+ T cells with an increased cytotoxic potential. Proc. Natl. Acad. Sci 117, 6686–6696 (2020). [PubMed: 32161126]
26. Bergamaschi L. et al. Longitudinal analysis reveals that delayed bystander CD8+ T cell activation and early immune pathology distinguish severe COVID-19 from mild disease. Immunity 54, 1257–1275.e8 (2021). [PubMed: 34051148]
27. Bangs SC et al. Human CD4+ Memory T Cells Are Preferential Targets for Bystander Activation and Apoptosis. J. Immunol 182, 1962–1971 (2009). [PubMed: 19201849]
28. White JT, Cross EW & Kedl RM Antigen-inexperienced memory CD8+ T cells: where they come from and why we need them. Nat. Rev. Immunol 17, 391–400 (2017). [PubMed: 28480897]
29. Maurice NJ, Taber AK & Prlic M The Ugly Duckling Turned to Swan: A Change in Perception of Bystander-Activated Memory CD8 T Cells. J. Immunol 206, 455–462 (2021). [PubMed: 33468558]
30. Abers MS et al. An immune-based biomarker signature is associated with mortality in COVID-19 patients. JCI Insight 6,144455 (2021). [PubMed: 33232303]
31. Herndler-Brandstetter D. et al. Post-thymic regulation of CD5 levels in human memory T cells is inversely associated with the strength of responsiveness to interleukin-15. Hum. Immunol 72, 627–631(2011). [PubMed: 21539877]
32. Jacomet F. et al. Evidence for eomesodermin-expressing innate-like CD8+ KIR/NKG2A+ T cells in human adults and cord blood samples. Eur. J. Immunol 45, 1926–1933 (2015). [PubMed: 25903796]
33. Jin J-H et al. Virtual memory CD8+ T cells restrain the viral reservoir in HIV-1-infected patients with antiretroviral therapy through derepressing KIR-mediated inhibition. Cell. Mol. Immunol 17, 1257–1265 (2020). [PubMed: 32210395]
34. Yang J, Zhu H, Murphy TL, Ouyang W & Murphy KM IL-18–stimulated GADD45β required in cytokine-induced, but not TCR-induced, IFN-γ production. Nat. Immunol 2, 157–164 (2001). [PubMed: 11175814]

35. Kastenmüller W, Torabi-Parizi P, Subramanian N, Lämmermann T & Germain RN A spatially-organized multicellular innate immune response in lymph nodes limits systemic pathogen spread. Cell 150, 1235–1248 (2012). [PubMed: 22980983]

36. Wimmers F. et al. The single-cell epigenomic and transcriptional landscape of immunity to influenza vaccination. Cell 184, 3915–3935.e21 (2021). [PubMed: 34174187]

37. Debisarun PA et al. Induction of trained immunity by influenza vaccination - impact on COVID-19. PLoS Pathog. 17, e1009928 (2021). [PubMed: 34695164]

38. Arunachalam PS et al. Systems biological assessment of immunity to mild versus severe COVID-19 infection in humans. Science 369, 1210–1220 (2020). [PubMed: 32788292]

39. Schulte-Schrepping J. et al. Severe COVID-19 Is Marked by a Dysregulated Myeloid Cell Compartment. Cell 182, 1419–1440.e23 (2020). [PubMed: 32810438]

40. Pérez-Gómez A. et al. Dendritic cell deficiencies persist seven months after SARS-CoV-2 infection. Cell. Mol. Immunol 18, 2128–2139 (2021). [PubMed: 34290398]

41. Phetsouphanh C. et al. Immunological dysfunction persists for 8 months following initial mild-to-moderate SARS-CoV-2 infection. Nat. Immunol 1–7 (2022) doi:10.1038/s41590-021-01113-x. [PubMed: 34789862]

42. Utrero-Rico A. et al. Alterations in Circulating Monocytes Predict COVID-19 Severity and Include Chromatin Modifications Still Detectable Six Months after Recovery. Biomedicines 9, 1253 (2021). [PubMed: 34572439]

43. You M. et al. Single-cell epigenomic landscape of peripheral immune cells reveals establishment of trained immunity in individuals convalescing from COVID-19. Nat. Cell Biol 23, 620–630 (2021). [PubMed: 34108657]

44. Klein SL & Flanagan KL Sex differences in immune responses. Nat. Rev. Immunol 16, 626–638 (2016). [PubMed: 27546235]

45. Patel AA et al. The fate and lifespan of human monocyte subsets in steady state and systemic inflammation. J. Exp. Med 214, 1913–1923 (2017). [PubMed: 28606987]

46. Cheong J-G et al. Epigenetic Memory of COVID-19 in Innate Immune Cells and Their Progenitors. 2022.02.09.479588 Preprint at 10.1101/2022.02.09.479588 (2022).

47. Tough DF, Borrow P & Sprent J Induction of Bystander T Cell Proliferation by Viruses and Type I Interferon in Vivo. Science 272, 1947–1950 (1996). [PubMed: 8658169]

48. Takahashi T. et al. Sex differences in immune responses that underlie COVID-19 disease outcomes. Nature 588, 315–320 (2020). [PubMed: 32846427]

49. Scully EP et al. Sex and Gender Differences in Testing, Hospital Admission, Clinical Presentation, and Drivers of Severe Outcomes From COVID-19. Open Forum Infect. Dis 8, ofab448 (2021). [PubMed: 34584899]

50. Tsang JS et al. Global Analyses of Human Immune Variation Reveal Baseline Predictors of Postvaccination Responses. Cell 157, 499–513 (2014). [PubMed: 24725414]

51. Kotliarov Y. et al. Broad immune activation underlies shared set point signatures for vaccine responsiveness in healthy individuals and disease activity in patients with lupus. Nat. Med 26, 618–629 (2020). [PubMed: 32094927]

## Methods and Extended Data Figure References

52. Harris PA et al. Research electronic data capture (REDCap)—A metadata-driven methodology and workflow process for providing translational research informatics support. J. Biomed. Inform 42, 377–381 (2009). [PubMed: 18929686]

53. Harris PA et al. The REDCap consortium: Building an international community of software platform partners. J. Biomed. Inform 95, 103208 (2019). [PubMed: 31078660]

54. Ravichandran S. et al. Antibody signature induced by SARS-CoV-2 spike protein immunogens in rabbits. Sci. Transl. Med 12, eabc3539 (2020). [PubMed: 32513867]

55. Ravichandran S. et al. Longitudinal antibody repertoire in ‘mild’ versus ‘severe’ COVID-19 patients reveals immune markers associated with disease severity and resolution. Sci. Adv 7, eabf2467 (2021). [PubMed: 33674317]

56. Tang J. et al. Antibody affinity maturation and plasma IgA associate with clinical outcome in hospitalized COVID-19 patients. Nat. Commun 12, 1221 (2021). [PubMed: 33619281]
57. Khurana S. et al. MF59 adjuvant enhances diversity and affinity of antibody-mediated immune response to pandemic influenza vaccines. Sci. Transl. Med 3, 85ra48 (2011).
58. Khurana S. et al. Human antibody repertoire after VSV-Ebola vaccination identifies novel targets and virus-neutralizing IgM antibodies. Nat. Med 22, 1439–1447 (2016). [PubMed: 27798615]
59. Khurana S. et al. Repeat vaccination reduces antibody affinity maturation across different influenza vaccine platforms in humans. Nat. Commun 10, 3338 (2019). [PubMed: 31350391]
60. De Biasi S. et al. Marked T cell activation, senescence, exhaustion and skewing towards TH17 in patients with COVID-19 pneumonia. Nat. Commun 11, 3434 (2020). [PubMed: 32632085]
61. Heit A. et al. Vaccination establishes clonal relatives of germinal center T cells in the blood of humans. J. Exp. Med 214, 2139–2152 (2017). [PubMed: 28637884]
62. Park LM, Lannigan J & Jaimes MC OMIP-069: Forty-Color Full Spectrum Flow Cytometry Panel for Deep Immunophenotyping of Major Cell Subsets in Human Peripheral Blood. Cytom. Part J. Int. Soc. Anal. Cytol 97, 1044–1051 (2020).
63. Bolger AM, Lohse M & Usadel B Trimmomatic: a flexible trimmer for Illumina sequence data. Bioinforma. Oxf. Engl 30, 2114–2120 (2014).
64. Liao Y, Smyth GK & Shi W featureCounts: an efficient general purpose program for assigning sequence reads to genomic features. Bioinforma. Oxf. Engl 30, 923–930 (2014).
65. Law CW, Chen Y, Shi W & Smyth GK voom: Precision weights unlock linear model analysis tools for RNA-seq read counts. Genome Biol. 15, R29 (2014). [PubMed: 24485249]
66. Risso D, Ngai J, Speed TP & Dudoit S Normalization of RNA-seq data using factor analysis of control genes or samples. Nat. Biotechnol 32, 896–902 (2014). [PubMed: 25150836]
67. Kang HM et al. Multiplexed droplet single-cell RNA-sequencing using natural genetic variation. Nat. Biotechnol 36, 89–94 (2018). [PubMed: 29227470]
68. Mulè MP, Martins AJ & Tsang JS Normalizing and denoising protein expression data from droplet-based single cell profiling. Nat. Commun 13, 2099 (2022). [PubMed: 35440536]
69. Stuart T. et al. Comprehensive Integration of Single-Cell Data. Cell 177, 1888–1902.e21 (2019). [PubMed: 31178118]
70. Martin MD & Badovinac VP Defining Memory CD8 T Cell. Front. Immunol 9, 2692 (2018). [PubMed: 30515169]
71. Zheng GXY et al. Massively parallel digital transcriptional profiling of single cells. Nat. Commun 8, 14049 (2017). [PubMed: 28091601]
72. Borcherding N, Bormann NL & Kraus G scRepertoire: An R-based toolkit for single-cell immune receptor analysis. F1000Research 9, 47 (2020). [PubMed: 32789006]
73. Gu Z, Gu L, Eils R, Schlesner M & Brors B circlize Implements and enhances circular visualization in R. Bioinforma. Oxf. Engl 30, 2811–2812 (2014).
74. Hastie T, Tibshirani R, Narasimhan B & Chu G impute: impute: Imputation for microarray data. R package version 1.72.1. (2022).
75. Hoffman GE & Roussos P Dream: powerful differential expression analysis for repeated measures designs. Bioinforma. Oxf. Engl 37, 192–201 (2021).
76. Wu T. et al. clusterProfiler 4.0: A universal enrichment tool for interpreting omics data. Innov. N. Y. N 2, 100141 (2021).
77. Liberzon A. et al. Molecular signatures database (MSigDB) 3.0. Bioinformatics 27, 1739–1740 (2011). [PubMed: 21546393]
78. Li S. et al. Molecular signatures of antibody responses derived from a systems biology study of five human vaccines. Nat. Immunol 15, 195–204 (2014). [PubMed: 24336226]
79. Monaco G. et al. RNA-Seq Signatures Normalized by mRNA Abundance Allow Absolute Deconvolution of Human Immune Cell Types. Cell Rep. 26, 1627–1640.e7 (2019). [PubMed: 30726743]
80. McCarthy DJ, Chen Y & Smyth GK Differential expression analysis of multifactor RNA-Seq experiments with respect to biological variation. Nucleic Acids Res. 40, 4288–4297 (2012). [PubMed: 22287627]

81. Hänzelmann S, Castelo R & Guinney J GSVA: gene set variation analysis for microarray and RNA-seq data. BMC Bioinformatics 14, 7 (2013). [PubMed: 23323831]

82. Ritchie ME et al. limma powers differential expression analyses for RNA-sequencing and microarray studies. Nucleic Acids Res. 43, e47 (2015). [PubMed: 25605792]

83. Love MI, Huber W & Anders S Moderated estimation of fold change and dispersion for RNA-seq data with DESeq2. Genome Biol. 15, 550 (2014). [PubMed: 25516281]

84. Gu Z, Eils R & Schlesner M Complex heatmaps reveal patterns and correlations in multidimensional genomic data. Bioinforma. Oxf. Engl 32, 2847–2849 (2016).

85. Candia J & Tsang JS eNetXplorer: an R package for the quantitative exploration of elastic net families for generalized linear models. BMC Bioinformatics 20, 189 (2019). [PubMed: 30991955]

86. Rosati E. et al. Overview of methodologies for T-cell receptor repertoire analysis. BMC Biotechnol. 17, 61 (2017). [PubMed: 28693542]

87. Morris EK et al. Choosing and using diversity indices: insights for ecological applications from the German Biodiversity Exploratories. Ecol. Evol 4, 3514–3524 (2014). [PubMed: 25478144]

88. Nakaya HI et al. Systems biology of vaccination for seasonal influenza in humans. Nat. Immunol 12, 786–795 (2011). [PubMed: 21743478]

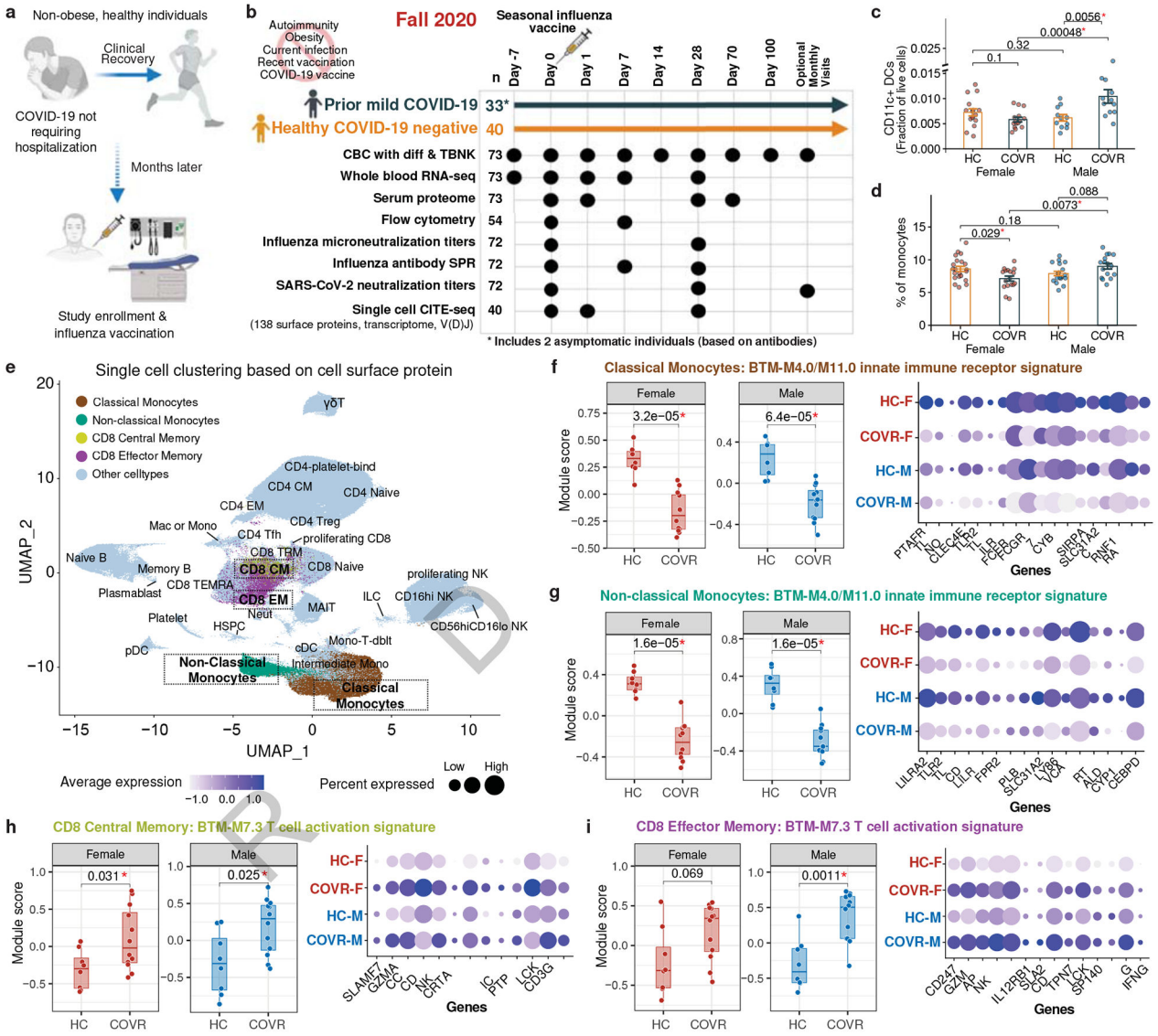


**Figure 1. Study overview and baseline differences.**

**a**, Schematic showing the study concept and design.

**b**, Data generated in the study. Both COVID-19-recovered (COVR) subjects and healthy controls (HC) were enrolled at seven days before vaccination (Day −7) and sampled at the indicated timepoints relative to the day of influenza vaccination. The number of subjects assayed for each data type is indicated. CBC with diff = complete blood count with differential; TBNK = T- and B-lymphocyte and Natural Killer cell phenotyping; SPR = Surface plasmon resonance.

**c**, Bar plots comparing the proportion of CD11c+ dendritic cells (DCs; as the fraction of live cells from flow cytometry) between COVR females (COVR-F; n=15), HC females (HC-F; n=16), COVR males (COVR-M; n=12), and HC males (HC-M; n=11) at day 0 (D0). The statistical significance is determined by two-tailed Wilcoxon test. Error bars indicate the standard error of each group.

**d**, Similar to (**c**) but for monocytes (from CBC; y-axis) between COVR-F (n=17), COVR-M (n=16), HC-F (n=21), and HC-M (n=19) at baseline (average of Day −7 and D0).
**e**, UMAP of the CITE-seq single cell data showing clustering of cells based on the expression of cell surface protein markers (632,100 single cells from all timepoints with CITE-seq data: days 0, 1, 28). Colored and boxed cell clusters are further explored in (**f-i**).
**f**, (left) Box plots comparing the innate immune receptor signature scores (see Methods) between HC-F (n=8) and COVR-F (n=12) (left box) and HC-M (n=8) and COVR-M (n=12) (right box) using the CITE-seq classical monocyte pseudobulk expression data at D0. Each point represents a subject. (right) Bubble plot showing the average gene expression of selected genes, including those in the Gene Ontology (GO) “pattern recognition receptor activity” and “immune receptor activity” gene sets.
**g**, Similar to (**f**) but showing the non-classical monocyte population at D0.
**h**, Similar to (**f**) but showing the T-cell activation (BTM-M7.3) module scores of CD8+ central memory T cells at D0. Bubble plot showing the average gene expression of the selected genes shared by male and female from the gene set enrichment analysis (see Methods).
**i**, Similar to (**h**) but showing the CD8+ T-cell effector memory population at D0.
All box plots show the median, first and third quantiles (lower and upper hinges) and smallest [lower hinge – 1.5× interquartile range (IQR)] and largest (upper hinge + 1.5× IQR) values (lower and upper whiskers). Unless otherwise noted, statistical significance of difference between groups is determined by two-tailed Wilcoxon test.

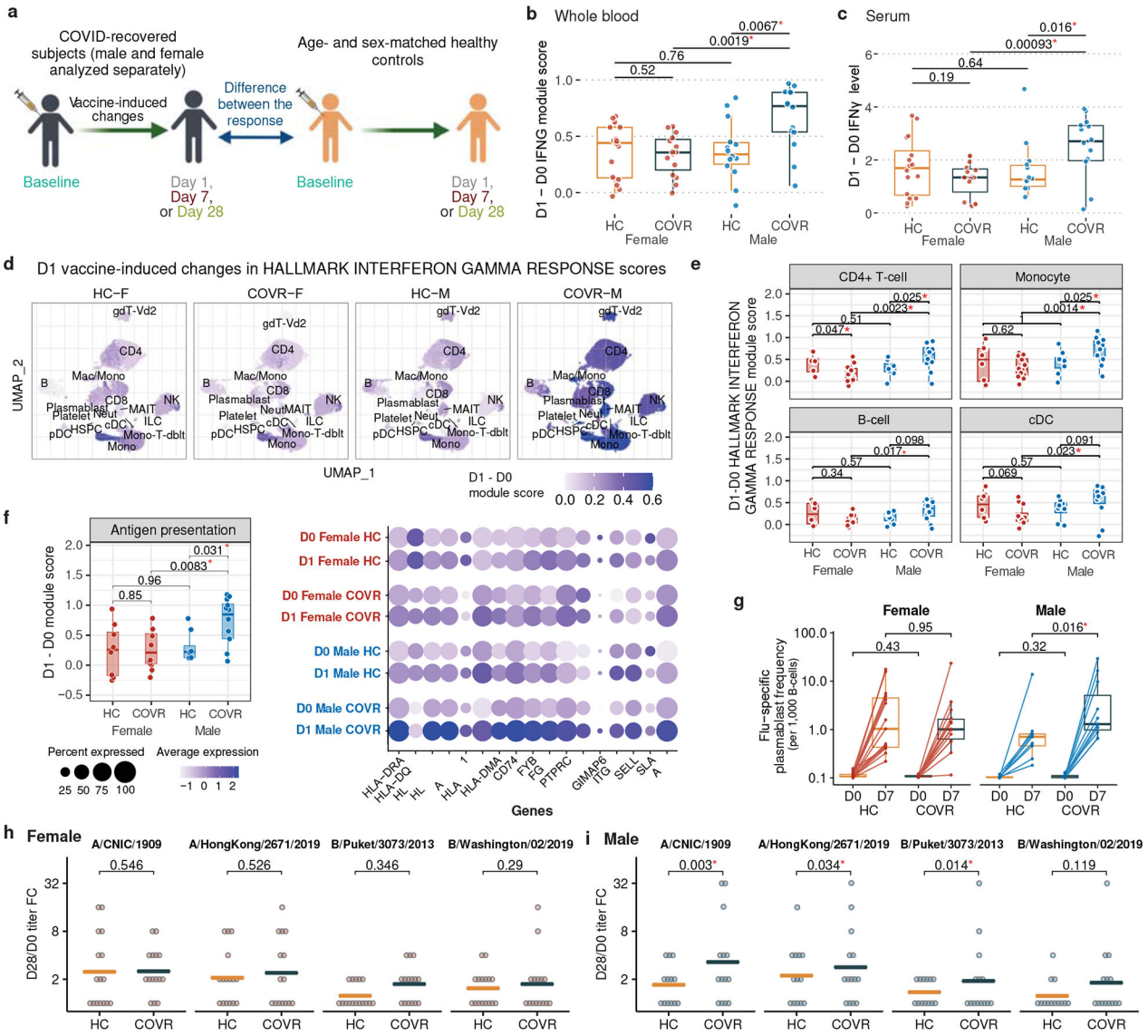


**Figure 2. Sex-specific response differences to influenza vaccination in COVID-19-recovered individuals and matching controls.**

**a**, Schematic of the sex-specific comparisons of vaccine induced changes from baseline at timepoints post vaccination (D1, D7, and D28) between COVR and HC subjects. Analyses applied to subjects under 65 years of age (see Methods).

**b**, Box plots of the D1 Interferon Gamma (IFNγ) transcriptional response score (D1 – D0, computed using genes from the Hallmark "Interferon Gamma Response" gene set) for COVR-F (n=15), COVR-M (n=14), HC-F (n=16), and HC-M (n=14).

**c**, Box plots of the D1 response (D1 – D0) of serum IFNγ protein level for the subjects shown in (**b**).

**d**, Surface protein expression-based UMAP (as in Fig. 1e) with cells colored by the D1 IFNγ transcriptional response score (D1 – D0; see (**b**) for the gene set used) within each cell subset for HC-F (n=8), COVR-F (n=12), and HC-M (n=8), COVR-M (n=12). Darker color indicates a greater difference between D1 and D0 for the indicated cell subset.

**e**, Similar to (**b**), but for the indicated cell subsets (computed using the CITE-seq pseudobulk mRNA expression data for the cell subset) in HC-F (n=8), COVR-F (n=12), HC-M (n=8) and COVR-M (n=12). cDC = conventional/myeloid dendritic cells.

**f**, (left) Box plot showing the D1 transcriptional response score (D1 – D0) of the antigen presentation related genes in classical monocytes for the same subjects in (**e**) (see Methods). (right) Bubble plot showing the averaged expression of individual leading-edge genes (LEGs) from the antigen presentation genes (see Methods) in classical monocytes.

**g**, Influenza-specific plasmablast (PB; All HA+ CD27+CD38+CD20$^{low}$CD21$^{low}$; see Methods and Supplementary Fig. 3) frequencies at D7 and D0, plotted separately for COVR-F (n=14), HC-F (n=15), COVR-M (n=11), and HC-M (n=9). Lines connect data points from the same subject at D0 and D7.

**h**, Analysis of the D28/D0 microneutralization titer fold-change (FC) for each of the four strains in the seasonal influenza vaccine (columns) in COVR-F and HC-F. Each dot represents one individual. The orange and grey lines indicate the average fold change for the HC-F and COVR-F, respectively. Unadjusted p values are derived from generalized linear models accounting for age, race, influenza vaccination history and baseline influenza titers (see Methods).

**i**, Similar to (**h**), but for COVR-M and HC-M.

All box plots show the median, first and third quantiles (lower and upper hinges) and smallest (lower hinge – 1.5× interquartile range (IQR)) and largest (upper hinge + 1.5× IQR) values (lower and upper whiskers). Unadjusted p values are shown. Unless otherwise noted, statistical significance of difference between groups is determined by two-tailed Wilcoxon test.

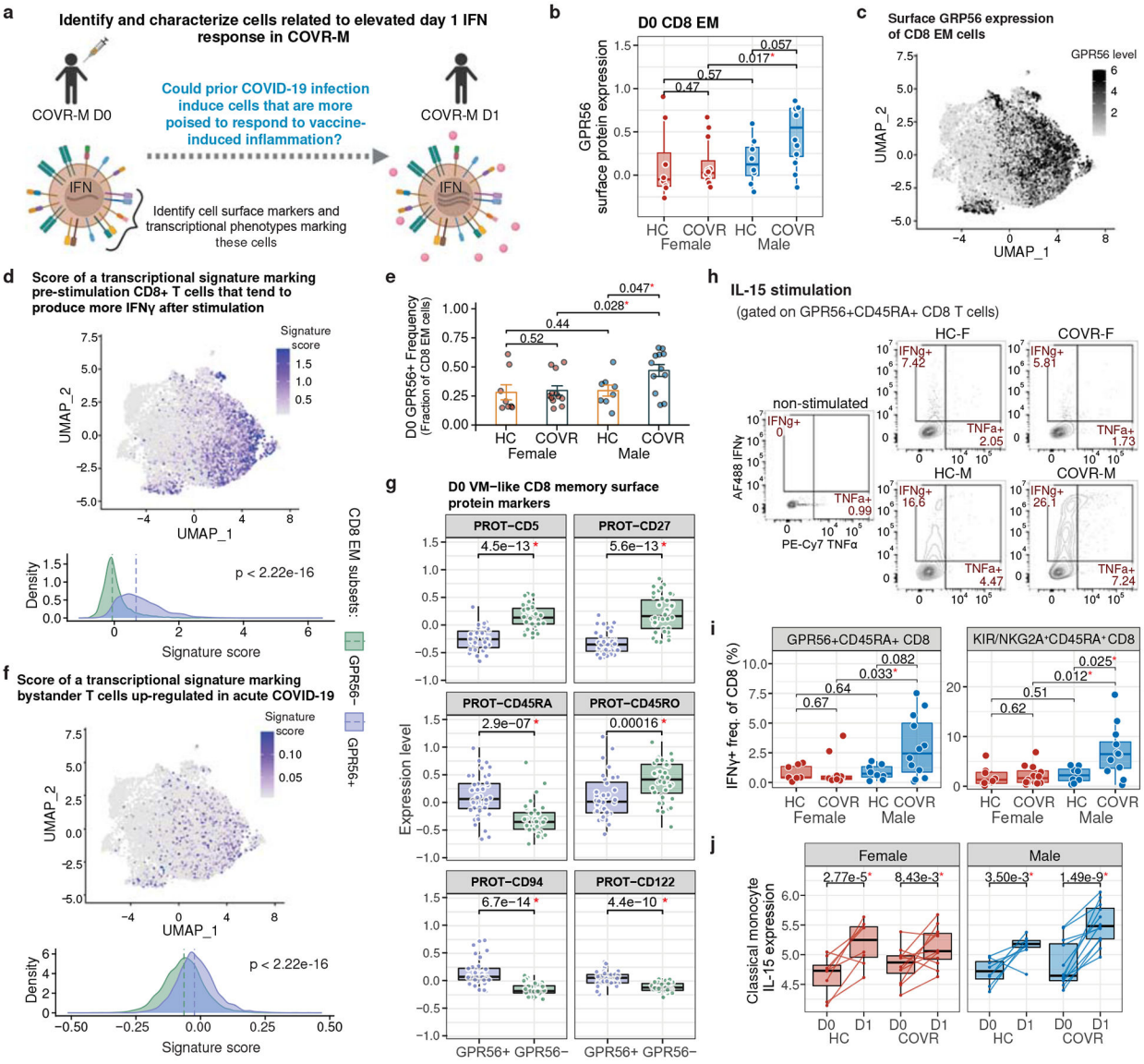


**Figure 3. Contributors to increased day 1 IFNγ responses in COVID-19-recovered males.**

**a**, Schematic illustrating the study questions regarding why COVR-M had elevated early IFNγ responses.

**b**, Box plots comparing the sample means of GPR56 surface expression in CD8+ effector memory T-cells (CD8+ EM) at D0 for COVR-F (n=12), HC-F (n=8), COVR-M (n=12), and HC-M (n=8).

**c**, UMAP of the D0 surface GPR56 protein expression on CD8+ EM from all 40 subjects with CITE-seq data. UMAP was derived using the top 60 variable surface proteins within the CD8+ EM cells (see Methods).

**d**, (top) Same UMAP as (**c**) but showing the D0 gene-expression signature score computed using genes associated with CD29$^{hi}$ CD8+ T-cells identified earlier in an independent study (Nicolet *et al*[23], see Methods). (bottom) Density plot showing the distribution of signature score above in the GPR56+ and GPR56− CD8+ EM. Dashed line indicates the median of the

distribution. Significance of the difference between the medians is determined by two-tailed Wilcoxon test at single-cell level.

**e**, Bar plots comparing the proportion of GRP56+ cells (as fractions of CD8+ EM in the CITE-seq data) between the same subjects as in **(b)** at D0. Significance is determined by two-tailed Wilcoxon test. Error bars indicate the standard error of each group.

**f**, Similar to (d) but showing the bystander T-cell signature score at baseline (D0) (signature genes originated from Bangs *et al*[27] and Bergamaschi *et al*[26], see Methods).

**g**, Box plots comparing the average expression of the indicated cell surface protein markers for the GPR56+ versus GPR56− CD8+ EM at D0 for the same subjects as in (**c**). Each point represents a subject.

**h,** Representative flow-cytometry contour plots of IFN$\gamma^+$ and TNF$\alpha^+$ gates within GPR56$^+$ CD45RA$^+$ CD8+ T-cells after IL-15 stimulation *in vitro* in the indicated groups. The number shown for each gate denotes the percent of parent (i.e., GPR56$^+$ CD45RA$^+$ CD8+ T-cells).

**i,** Boxplots showing the frequencies of IFN$\gamma$+ GPR56+ CD45RA+ VM-like CD8+ T-cells (left, as fractions of CD8+ T-cells) and IFN$\gamma$+ KIR/NKG2A+ CD45RA+ CD8+ T-cells (right, as fractions of CD8+ T-cells) in the same subjects as in **(b)** after IL-15 stimulation *in vitro*.

**j,** Box plots comparing D0 and D1 pseudobulk IL-15 mRNA expression (y-axis) in classical monocytes for the same subjects as in **(b)**. Significance is determined by a linear model accounting for age, race, and influenza vaccination history (see Methods).

All box plots show the median, first and third quantiles (lower and upper hinges) and smallest (lower hinge – 1.57× interquartile range (IQR)) and largest (upper hinge + 1.5× IQR) values (lower and upper whiskers). Unless otherwise noted, statistical significance of difference between groups is determined by two-tailed Wilcoxon test.

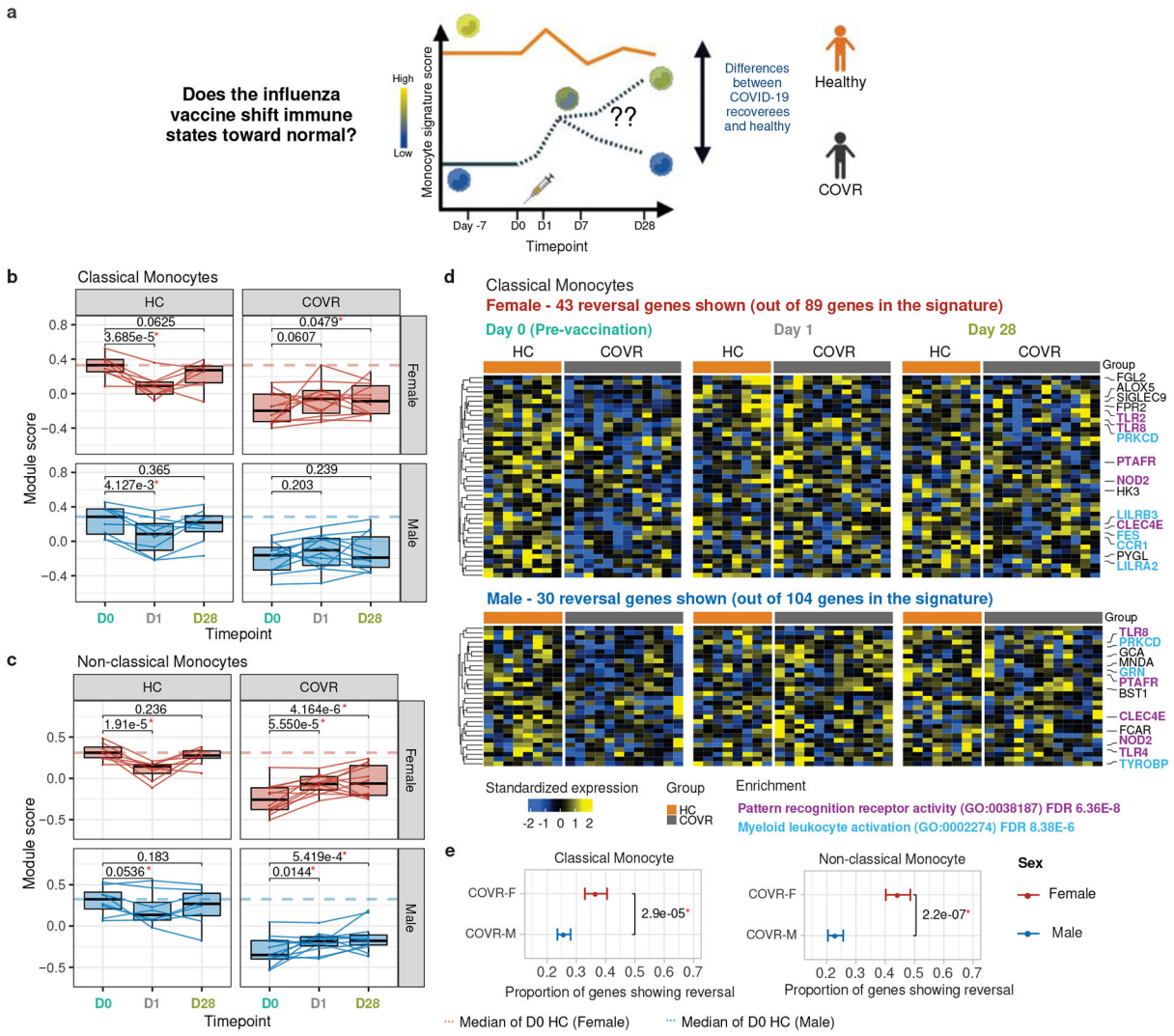


**Figure 4. Post mild COVID-19 gene expression imprints in monocytes shifted by influenza vaccination.**

**a**, Schematic showing the study questions.

**b**, Box plots showing the module scores of the innate immune receptor (IIR) signature (see Fig. 1f) in HC-F (n=8), HC-M (n=8), COVR-F (n=12) and COVR-M (n=12) at D0, D1 and D28 using the CITE-seq pseudobulk gene expression data in classical monocytes. The dashed line represents the median D0 score of the HCs of the same sex. Lines connect data points from the same subject at different timepoints. Statistical significance of differences is determined by a mixed-effects model accounting for age, race, and influenza vaccination history (see Methods). Unadjusted p values are shown.

**c,** Similar to (**b**) but for non-classical monocytes (see Fig. 1g).

**d**, Heatmap showing the expression of the "reversal" genes in classical monocytes (row-standardized; see Extended Data Fig. 5c for non-classical monocytes). Reversal genes are defined as those genes in the baseline IIR signature (see also Fig. 1f) whose expression in COVR subjects at D1 and D28 after vaccination moved towards the baseline (pre-vaccination) expression of HCs. COVR-F (top) and COVR-M (bottom) shown separately;

HC are also included for comparison. The rows are genes and columns are individual samples (grouped by subject/timepoint) with timepoint and subject group labels shown at the top, including the same subjects as in **(b)** at each timepoint. The names of genes that belong to gene sets of functional interest are shown (FDR-corrected enrichment p values are shown).

**e,** Comparison of the proportion of IIR signature genes (see Fig. 1f,g) that show partial reversal in COVR-F versus COVR-M in classical and non-classical monocytes. The mean and 95% confidence intervals (denoted by the bars) are derived from a bootstrapping procedure (see Methods). Significance is determined by the two-tailed Wilcoxon test between the bootstrapped samples.

All box plots show the median, first and third quantiles (lower and upper hinges) and smallest (lower hinge – 1.5× interquartile range (IQR)) and largest (upper hinge + 1.5× IQR) values (lower and upper whiskers).